Journal of Materials Research and Technology 43 (2026) 6029–6052

Contents lists available at ScienceDirect

Journal of Materials Research and Technology

journal homepage: www.elsevier.com/locate/jmrt

Finite element simulations and experimental validation of LENS-deposited IN625 yield surface identification under sequential tension/compression–torsion probing using a novel anisotropic UMAT framework

Pankaj Kumar [a,*], Ved Prakash Dubey [a], Tomasz Durejko [b], Xiaochuan Liu [c], Mateusz Kopec [a,d,**], Zbigniew L. Kowalewski [a]

[a] Institute of Fundamental Technological Research, Polish Academy of Sciences, Warsaw, Poland
[b] Institute of Materials Science and Engineering, Military University of Technology, Kaliskiego 2 Str., 00-908, Warsaw, Poland
[c] Xi'an Jiaotong University, Xianning West Road, Xi'an, Shaanxi, 710049, China
[d] College of Science and Engineering, University of Derby, Markeaton Street, Derby, DE22 3AW, UK

ARTICLE INFO

Keywords:
Inconel 625
Anisotropic yield surface
Szczepiński yield criterion
User subroutine
Kinematic hardening
Sequential multiaxial loading

ABSTRACT

Anisotropic yield criteria and kinematic hardening laws have been independently validated for additively manufactured alloys. However, their specific combination has not been implemented in a finite element user subroutine and validated against 360° sequential biaxial probing data for LENS-deposited nickel-base alloys. Present work delivers the first validated implementation of this coupling for LENS-deposited Inconel 625, combining the Szczepiński quadratic yield criterion with Armstrong–Frederick kinematic hardening. The implemented return-mapping algorithm accumulates the plastic multiplier across Newton–Raphson iterations before updating the plastic and equivalent plastic strain state variables. This distinction is significant for the non-radially-symmetric Szczepiński surface where the flow direction rotates at each iteration unlike the fixed radial direction of isotropic return mapping. A two-step iterative boundary-condition correction scheme ensures each probing direction converges within $\pm 1.5^{\circ}$ of the experimental stress angle, achieved for 16 of 17 sequential paths. Path P1, the virgin specimen opening probe retains a residual angular deviation of -2.97° due to absent accumulated back-stress at the start of the sequential cycle. The validated UMAT reproduces all 17 directional yield points with a mean absolute angular error of 0.86°, mean absolute axial and shear stress deviations of 11.4 MPa and 12.5 MPa, respectively. Path-level deviations reach a maximum of 32 MPa in axial stress at P10 and 41.4 MPa in shear stress at P5, attributed to angular misalignment between back-stress and probing direction in the compressive–shear and near-pure-torsion sectors, respectively. This establishes the framework as a computational tool for characterising multiaxial yield surface under complex loading.

1. Introduction

Nickel-based alloys fabricated via Laser Engineered Net Shaping (LENS) are increasingly deployed in structurally critical components such as aerospace turbine hardware, biomedical implants, and repair tooling [1,2]. The layer-by-layer thermal cycling inherent to LENS processing induces a pronounced columnar grain morphology and build-direction-dependent mechanical anisotropy in Inconel 625 (IN625), rendering isotropic yield criteria fundamentally inadequate for predicting plastic onset under generalised stress states. Sharp thermal gradients during rapid solidification promote the formation of columnar grains with a strong ⟨001⟩//deposition-axis crystallographic fibre texture, while inter-layer sintering sequences progressively redistribute solute elements and introduce build-direction-dependent dislocation sub-structures [1,3]. These features collectively produce a noticeable mechanical anisotropy, manifested in the directional resistance to plastic flow and the yield threshold vary substantially with both the loading direction and the accumulated plastic strain history. A pronounced Bauschinger effect [4,5] further modifies this effect where pre-straining in one direction lowers the yield threshold upon reversal in

* Corresponding author.
** Corresponding author. Institute of Fundamental Technological Research, Polish Academy of Sciences, Warsaw, Poland.
E-mail addresses: pkumar@ippt.pan.pl (P. Kumar), mkopec@ippt.pan.pl (M. Kopec).

https://doi.org/10.1016/j.jmrt.2026.07.136
Received 15 June 2026; Received in revised form 15 July 2026; Accepted 17 July 2026
Available online 24 July 2026

the opposite direction. Consequently, the elastic domain is not merely scaled but translated, distorted, and rotated in multiaxial stress space [6]. To capture these phenomena at the fundamental level, it is necessary to characterise the material response directly through the multiaxial yield surface instead of scalar yield stress evaluated from a single uniaxial tensile test. The classical isotropic Huber-Von Mises-Hencky criterion [5], which predicts a perfect circle centred at the stress space origin, is explicitly inadequate for textured, AM alloys because it applies both isotropy and centrosymmetry i.e. equal tensile and compressive yield thresholds, two conditions simultaneously violated by LENS-deposited IN625.

The theoretical and experimental foundations of plasticity-based frameworks for path-dependent materials have evolved progressively over more than a century of sustained research. The historical foundation was established by Bauschinger [7,8], who observed that Bessemer steel, after plastic deformation in tension, exhibited a markedly reduced yield stress upon subsequent compression. This direction-dependent asymmetry, known as the Bauschinger effect, demonstrated for the first time that the yield limit is not a fixed scalar but is inherently sensitive to the direction and history of prior plastic deformation. Von Mises [5,9] formalised this understanding by developing a general yield function for polycrystalline materials, which remains the standard isotropic reference surface in modern plasticity. Later on, Prager [10] introduced the back-stress tensor as a tensorial internal variable that translates the yield surface rigidly in stress space providing the first physically motivated constitutive description of kinematic hardening under multiaxial loading. Further, Armstrong and Frederick (1966) [4,11] enriched Prager's model by incorporating a dynamic recovery term that drives the back-stress to a direction-dependent saturation limit. This enables the simulation of ratcheting and mean stress relaxation under cyclic and non-proportional loading histories, precisely the loading regime central to the sequential probing method employed in present work.

Recognising the inadequacy of translational and isotropic yield models for textured and pre-deformed materials, Szczepiński [5] proposed an anisotropic yield criterion for multiaxial stress states based on a second-order quadratic formulation incorporating linear stress terms. In the bi-directional axial-shear (σ, τ) stress space, the Szczepiński criterion requires only five independent material parameters for calibration of the yield surface represented by an elliptical function. Unlike Hill's [12] orthotropic yield criterion which imposes principal axis alignment with the material symmetry axes, the Szczepiński model simultaneously captures yield surface translation, distortion, and rotation. Consequently, the model is uniquely suited for LENS-deposited alloys in which the principal anisotropy axes may be misaligned with respect to the deposition direction due to scan-vector rotation between build layers [13,14]. Numerous experimental investigations [13–15] established the utility of the sequential single-specimen probing methodology for yield surface identification for various additive manufactured alloys. The methodology, which applies a series of short radial loading probes in an axial-shear stress plane to a thin-walled tubular specimen, each depositing a small controlled increment of equivalent plastic strain $\Delta\bar{\varepsilon}^{p}$, was systematically applied by Szczepinski and co-workers [5,16,17]. Later on, Dubey et al. [13] utilised the Szczepiński quadratic criterion with a least-squares fitting procedure to quantify ellipse centre shift and axis ratio from sequential biaxial probing data for conventional CP-Ti alloy.

The extension of kinematic hardening models to AM alloys has been an active research frontier over the past decade. Agius et al. [6] proposed an efficient modelling scheme for additive manufactured Ti–6Al–4V that combines the Hill [12] anisotropic yield function with Armstrong–Frederick kinematic hardening rule. They reported that superposition of multiple back-stress components is necessary to reproduce the Bauschinger effect and the cyclic stress-strain evolution across different build orientations. Geng and Harrison [18] utilised Crystal Plasticity Finite Element Modelling (CPFEM) to simulate functionally graded Ti–6Al–4V alloy. They demonstrated that microstructural gradients inherent in AM processes directly govern the activation of individual slip systems and the resulting shape of the yield locus under varying stress states. Complementing this, Somlo et al. [19] adopted a multiscale methodology based on CPFEM and periodic representative volume elements (RVEs) to simulate the direction-dependent behaviour of AM 316 L stainless steel and Ti–6Al–4V alloys. By incorporating crystallographic texture and columnar grain morphology, they calibrated Hill's [12] and YLD2004-18 P yield surface models and confirmed that AM-induced texture produces an anisotropy that can only be partially reproduced by Hill's model [12]. This behaviour motivated the use of more general quadratic criteria such as Szczepiński yield model for materials with significant shear-coupling terms. Notably, these CPFEM studies confirmed that they require accurate and extensive EBSD maps, single-crystal elastic constants and slip systems along with substantial computational expense for RVE averaging. These computational requirements impose significant limitations that the present phenomenological Szczepiński-UMAT approach explicitly circumvents by calibrating directly against specimen based experimental yield points. In pursuit of a related approach, Hu et al. [20] utilised Chaboche rate-dependent model [21] to predict subsequent yield surfaces of alloy steel under tension–torsion sequential loading. Their simulation results demonstrated that J_2-based classical models with combined isotropic–kinematic hardening can reproduce the experimental yield locus translation but systematically underestimate the ellipse distortion at large offset plastic strains. This finding directly motivated the acceptance of the non-circular Szczepiński surface in the present work, where the coupling coefficient and the anisotropy ratio produce a measurable ellipse inclination and aspect-ratio distortion that a J_2-based model cannot capture.

Despite these advances, a specific and unaddressed gap persists in the computational mechanics literature for AM nickel-base alloys. Hill-type UMATs have been implemented for AM Ti–6Al–4V but impose principal axis alignment with material symmetry axes, which is violated in LENS-deposited IN625 due to scan-vector rotation between build layers that misaligns the principal anisotropy axes [6]. YLD/Barlat-family criteria provide excellent sheet-forming accuracy but require six or more independent anisotropy coefficients obtained from multi-specimen biaxial tests an experimental burden incompatible with the single-specimen sequential probing protocol adopted here [19]. Chaboche-type combined isotropic–kinematic hardening models have been applied to alloy steel under tension–torsion, but J_2-based flow surfaces systematically underestimate ellipse distortion at large offset plastic strains, as demonstrated quantitatively by Hu et al. [20]. Crystal plasticity FEM approaches accurately resolve texture-induced anisotropy but require extensive EBSD characterisation, single-crystal constants, and RVE averaging, imposing computational costs that are disproportionate for phenomenological yield surface identification [19]. The present contribution is therefore not the introduction of a new constitutive concept, but the first validated transfer and deployment of the specific combination of (i) the Szczepiński five-parameter general quadratic yield criterion implemented in a 2D axial-shear UMAT, (ii) Armstrong–Frederick nonlinear kinematic hardening integrated via implicit Euler update, (iii) a plastic multiplier accumulation correction across Newton–Raphson iterations, and (iv) an iterative two-step boundary-condition correction scheme. It can be noted that the application of this constitutive law against 17 full 360° sequential biaxial probing paths on LENS-deposited IN625 has not been previously reported. Table 1 summarises the specific elements of the present contribution relative to the most closely related prior works, highlighting what is adopted from existing literature and what constitutes the novel combination delivered in this study.

As Table 1 clarifies, Dubey et al. [13] and Kopec et al. [15] applied the Szczepiński criterion purely as a curve-fitting tool to experimental data, without embedding it in a finite element UMAT capable of forward simulation. Agius et al. [6] coupled an anisotropic yield surface with

Table 1
Comparison of present contribution relative to closely related prior works.

Literature	Yield Criterion	Kinematic Hardening	Material	Validation Data
Agius et al. [6]	Hill (orthotropic)	Armstrong–Frederick	AM Ti–6Al–4V	Monotonic + cyclic uniaxial
Hu et al. [20]	J_2 Von Mises	Chaboche combined	Alloy steel	Tension–torsion sequential
Somlo et al. [19]	Hill + YLD2004	CPFEM	AM 316 L, Ti–6Al–4V	RVE texture averaging
Dubey et al. [13]	Szczepiński (fitted)	no FE-UMAT	CP-Ti	Sequential probing
Kopec et al. [15]	Szczepiński (fitted)	no FE-UMAT	AM 316 L	Sequential probing
Present work	Szczepiński (UMAT)	Armstrong–Frederick	LENS IN625	Sequential probing

Armstrong–Frederick hardening in ABAQUS, but for the Hill criterion under uniaxial cycling, not for the Szczepiński surface under full biaxial sequential probing. The present contribution is therefore not the introduction of a new constitutive concept, but the first validated transfer and deployment of specific coupling of Szczepiński yield criterion with Armstrong–Frederick hardening within a forward-simulating UMAT for LENS-deposited IN625 under a full 360° sequential biaxial probing technique, a material system and loading regime for which this combination has not previously been demonstrated.

In response to these gaps, the present work develops and validates a novel UMAT subroutine within ABAQUS software specifically designed to simulate the sequential evolution of the anisotropic yield surface of as-received LENS-deposited Inconel 625 under 17 sequential biaxial tension/compression–torsion probing paths spanning the full 360° of the (σ, τ) stress space. The subroutine implements the Szczepiński anisotropic yield criterion within a robust elastic predictor–plastic corrector return-mapping framework incorporating Armstrong–Frederick nonlinear kinematic hardening mechanism. A documented implementation practice ensures correct plastic multiplier accumulation across Newton–Raphson iterations for the non-radially-symmetric Szczepiński surface. This practice avoids a known failure mode in which only the final iterative correction is mistakenly treated as the total plastic multiplier. This correction confirms reliable identification of the 0.01% plastic strain offset yield point consistently across all 17 sequential loading paths. This investigation thereby addresses a significant gap in the computational mechanics of AM alloys, providing a validated, physically consistent, and computationally efficient numerical methodology for simulating multiaxial yield surface evolution in materials exhibiting AM-induced crystallographic anisotropy and path-dependent kinematic back-stress accumulation.

2. Materials and experimental methodology

The material studied in the present study was additively manufactured Inconel 625 (IN625) alloy. Thin-walled tubular specimens with an outer diameter of 12 mm and a length of 72 mm were fabricated using the LENS-MR7 system. The IN625 powder feedstock, supplied by Carpenter Additive, comprised a nominal chemical composition (wt.%) of balance Ni, 21 Cr, 9 Mo, 4 Nb, 5 Fe, 1 Co, 0.5 Si, 0.5 Mn, 0.4 Ti, 0.4 Al, 0.1 C, 0.015 S, and 0.015 P. Fabrication was conducted in a high-purity argon atmosphere with the build direction oriented vertically. The processing parameters employed during deposition were as follows: laser power of 380 W, layer thickness of 0.3 mm, hatch spacing of 0.45 mm, contour scanning speed of 14 mm/s, volume scanning speed of 15 mm/s, and powder feed rate of 11.2 RPM, corresponding to an approximate volumetric energy density of 200 J/mm^3. These parameters were optimized to obtain fully dense, thin walled tubular structure. After the AM process, the tubes were removed from the build plate using wire electrical discharge machining (WEDM) and subsequently machined to obtain the final specimen geometry shown in Fig. 1(a). The inner surface of the tubular specimens was finished using WEDM, whereas the outer surface was precision-machined by turning operation. The gauge section was finish machined prior to mechanical testing, though surface roughness was not quantitatively characterised. The specimen roughness is also specified on technical drawing of Fig. 1(a). All specimens were tested in the as-built condition without any post-build heat treatment, thereby preserving the columnar, texture-bearing microstructure inherent to the LENS deposition sequence.

Mechanical tests were performed at room temperature (23°C) using the MTS 858 servo-hydraulic biaxial testing machine with the maximum loading capacities of ±25 kN in axial force and ±100 Nm in torque. Uniaxial tensile tests were first carried out on three specimens at a constant strain rate of 0.00025 s^{-1} to determine the fundamental mechanical properties of the material. Subsequently, the yield points in the axial stress-shear stress space were experimentally determined using a sequential proportional loading methodology based on a single-specimen probing approach. This single-specimen strategy minimizes specimen-to-specimen variability while substantially reducing experimental cost and material consumption. However, an inherent limitation is the progressive accumulation of plastic deformation from preceding loading paths which may influence subsequent yield measurements. This effect was deliberately minimized by restricting each probing step to a small plastic offset strain of 0.01% and by adopting an appropriate sequence of loading directions for yield surface identification. The yield surface probing methodology consisted of a total of 17 proportional strain paths [13]. The loading sequence initiated in tension and progressed sequentially through the prescribed loading directions before

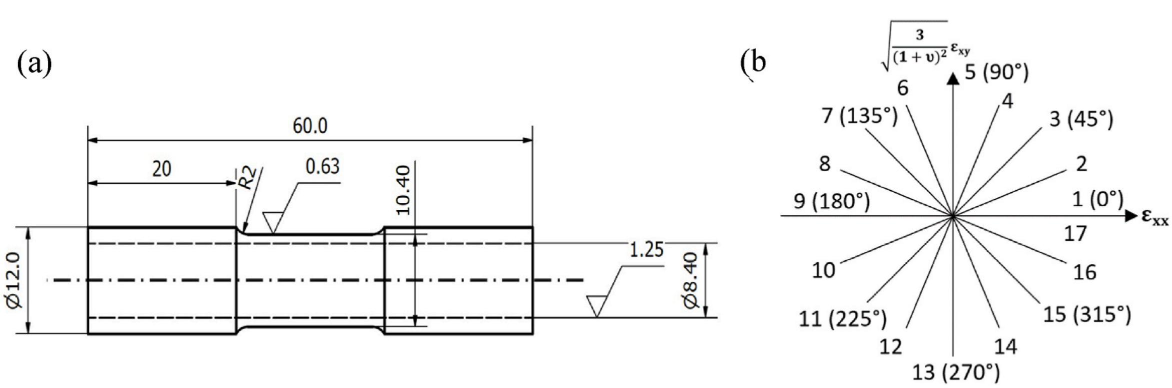

Fig. 1. (a) Schematic of the thin-walled tubular specimen and (b) loading sequence of strain paths for yield points determination in the biaxial strain space.

returning to tension in the same direction within $\left(\varepsilon_{xx}, \sqrt{\left(\frac{3}{(1+\nu)^2}\right)}\varepsilon_{xy}\right)$ strain space, as shown in Fig. 1(b), where ν is the Poisson's ratio. For each path, strain-controlled loading began from the origin and continued until a pre-defined small plastic offset strain was achieved. Then, the stress-controlled unloading process was executed until the force and torque reached zero values. Yield points corresponding to each loading direction were determined using the offset strain method, in which yielding was defined as the point where the equivalent stress-strain response deviated from the linear elastic response by 0.01%. To ensure accurate strain measurement and control during biaxial loading, Vishay 120 Ω strain gages were bonded at the mid-section of the outer surface of gauge region of the tubular specimens. Strain acquisition was performed using the manufacturer-specified gauge factors supplied with the strain gauges and no additional experimental gauge-factor calibration was required. Prior to testing, the measurement system was verified through standard bridge balancing and zeroing procedures. Axial and shear strain components were obtained from the three-element 45° rectangular rosette (EA-05-125RA-120) using the standard strain-transformation equations implemented in the Vishay strain acquisition system, while hoop strain was measured independently using a linear-pattern rosette (EA-13-062AK-120 The accuracy of the force, torque, and strain measurements was governed by the specifications of the MTS 858 biaxial testing system and the Vishay strain measurement system. To assess experimental repeatability, the complete sequential yield surface identification procedure was independently performed on three specimens. The resulting scatter in the identified yield points was quantified using the coefficient of variation (CV), which ranged from 1% to 6% across the individual loading paths. These relatively low CV values confirm good repeatability of the proposed experimental procedure and indicate that experimental scatter has a negligible influence on the identified initial yield surface. The experimental methodology adopted for precise multiaxial strain measurement and closed-loop strain control is described in detail by Dubey et al. [13,14].

3. Numerical methodology

Present study employs two distinct user-defined subroutines addressing two physically distinct regimes of the material response. Section 3.1 develops a VUMAT within Abaqus/Explicit to reproduce the large-strain, damage-coupled tensile response through to ductile fracture, governed by triaxiality-dependent void growth and mesh-regularised softening. Section 3.2 is focused mainly on development of UMAT within Abaqus/Standard to identify the anisotropic yield surface under small-offset (0.01% equivalent plastic strain) sequential biaxial probing, a regime in which damage evolution is by design absent. No single existing constitutive framework addresses both regimes simultaneously motivating the use of two different purpose-built subroutines. Both models share common elastic properties of Young's modulus, E and Poisson's ratio, ν. The resulting isotropic elastic stiffness tensors are calibrated once from the tensile test in Section 2 and applied identically in both subroutines. The plastic hardening and damage parameters calibrated for the tensile VUMAT are specific to the large-strain fracture problem and are not transferred to the Szczepiński-UMAT. Its five yield surface material parameters are instead calibrated independently from the sequential biaxial probing dataset.

3.1. Uniaxial tensile deformation

The FE-model developed is validated against experimental uniaxial tensile data obtained from LENS-deposited IN625 specimens fabricated and tested under the conditions described in Section 2. 3D finite element model of tubular tensile specimen similar to experimental one was created in ABAQUS having cylindrical gauge section of 20 mm with an outer and inner diameters of 10.4 and 8.4 mm respectively. The whole model is discretised using 8-node linear brick elements which generated uniform mesh with 6000 elements and 12121 nodes. A reasonably fine and structured mesh was generated in the gauge section to accurately capture the highly localised stress gradients, necking phenomena, and the rapid damage evolution during the post necking phase. Thereafter, boundary conditions were kept similar to the experimental procedure of uniaxial tensile test. The bottom circular face of the specimen was fully constrained in all directions. At the other end of the circular grip section, it was kinematically coupled with a central Reference Point (RP). At this RP, a displacement-controlled loading condition was applied. The applied displacement magnitude was set to exceed the experimentally observed failure displacement of LENS-deposited IN625 under all tested conditions. To validate that the simulation remained truly quasi-static, the energy balance was continuously monitored and the kinetic energy of the deforming specimen was verified to remain negligible compared to the internal strain energy throughout the deformation process prior to final fracture.

3.1.1. Constitutive model

The numerical model is adopted within the framework of continuum damage mechanics. Strain equivalence law is utilised to decouple the plasticity computations from the material degradation. This principle states that the deformation behaviour of a damaged material can be represented by the virgin material behaviour when the true macroscopic Cauchy stress tensor, σ_{ij}, is replaced by the effective stress tensor, $\widetilde{\sigma}_{ij}$ [22]:

$\widetilde{\sigma}_{ij} = \frac{\sigma_{ij}}{1-D}$ (1) In Equation (1), $\widetilde{\sigma}_{ij}$ represents effective Cauchy stress tensor, σ_{ij} stands for nominal (damaged) Cauchy stress tensor and D is a scalar isotropic damage variable, $0 \le D < 1$. For a given strain increment $\Delta\varepsilon_{ij}$, the trial effective Cauchy stress $\widetilde{\sigma}_{ij}^{tr}$ is computed using the undamaged isotropic elasticity tensor [4,22]:

$$\widetilde{\sigma}_{ij}^{tr} = \widetilde{\sigma}_{ij}^{n} + 2\mu\Delta\varepsilon_{ij} + \lambda\Delta\varepsilon_{kk}\delta_{ij} \tag{2}$$

In Equation (2), $\widetilde{\sigma}_{ij}^{n}$ is effective stress, $\Delta\varepsilon_{ij}$ is strain increment tensor, $\Delta\varepsilon_{kk}$ is volumetric strain increment, δ_{ij} is Kronecker delta, μ and λ are the Lamé constants, derived from the Young's modulus E and Poisson's ratio ν.

3.1.2. Yield criterion and plasticity framework

The onset of plastic flow is governed by the J_2 (Von Mises) yield criterion evaluated in the effective stress space. The yield function f is defined as [9]:

$f = \widetilde{q}^{tr} - \sigma_Y(\overline{\varepsilon}^{pl}) \le 0$ (3) In Equation (3), $\widetilde{q}^{tr} = \sqrt{\frac{3}{2}\widetilde{S}_{ij}^{tr}\widetilde{S}_{ij}^{tr}}$ is the trial effective Von Mises equivalent stress, $\widetilde{S}_{ij}^{tr}$ is the deviatoric component of the trial stress, and $\sigma_Y(\overline{\varepsilon}^{pl})$ is the flow stress (isotropic hardening) dependent on the equivalent plastic strain $\overline{\varepsilon}^{pl}$. It can be argued that if $f > 0$, the step is plastic. The J_2 plastic multiplier $\Delta\gamma$, which corresponds to the increment in equivalent plastic strain $\Delta\overline{\varepsilon}^{pl}$, is calculated via the radial return method [23]:

$\Delta\overline{\varepsilon}^{p} = \Delta\gamma_{J_2} = \frac{\widetilde{q}^{tr} - \sigma_Y(\overline{\varepsilon}^{pl})}{3\mu}$ (4) In Equation (4), $\Delta\gamma$ is distinct from the Lamé constant λ used in the elastic stiffness tensor and from the Hessian eigenvalues $\kappa_{1,}$ κ_2. Using Equation (4), the effective stress is then radially projected back onto the yield surface.

3.1.3. Damage initiation and evolution

Damage initiation is governed by a triaxiality-dependent critical plastic strain, $\varepsilon_c(\eta)$ following the Rice–Tracey void growth mechanism [24]:

$$\varepsilon_c(\eta) = \varepsilon_{c,0}\exp\left[-\alpha_e\left(\eta - \eta_{\text{ref}}\right)\right] \tag{5}$$

In Equation (5), $\varepsilon_{c,0}$ is the critical damage initiation strain at reference triaxiality, α_e is coefficient for triaxial state, $\eta = \frac{p}{\sigma_{VM}}$ stress triaxiality ratio where, $p = -(1/3)\cdot tr(\sigma)$ is the hydrostatic pressure. η_{ref} is the reference triaxial state of material. Henceforth, the ductile fracture by numerical procedure can be evidenced as elements at gauge section η accumulate fracture earlier, whereas outward elements fail thereafter. Once $\bar{\varepsilon}^{pl} \geq \varepsilon_c(\eta)$, damage progresses accordingly by softening law exponentially to remove mesh-dependency [25]:

$$h_{loc} = \frac{\sigma_Y \cdot \ell_c}{G_f} \tag{6}$$

In Equation (6), h_{loc} is local softening rate, σ_Y is current flow stress at damage onset, ℓ_c is the element characteristic length and G_f is the mode-I fracture energy. This confirms that the energy dissipated per unit fracture area equals G_f regardless of mesh size, rendering the load-displacement response mesh-independent. The damage variable can be defined as [22,26]:

$$D^{tgt} = 1 - \exp\left[-h_{loc}\left(\bar{\varepsilon}^{pl} - \varepsilon_{c,0}\right)\right] \tag{7}$$

In Equation (7), D^{tgt} is an unconstrained damage value where $D^{tgt} \geq D^n$ and D_n is irreversibility constraint. During rapid damage growth, the explicit solver tends to develop high-frequency stress oscillations. To mitigate this numerical instability, regularization scheme is utilised, which smoothen the damage evolution, as follows [26–28]:

$$D^{n+1} = D^n + \frac{D^{tgt} - D^n}{\Delta t + \mu_v}\Delta t \tag{8}$$

In Equation (8), D^{n+1} is regularised damage at new time step, μ_v is the viscous relaxation time. The updated nominal Cauchy stress is expressed as [26]:

$$\sigma_{ij}^{n+1} = \left(1 - D^{n+1}\right)\tilde{\sigma}_{ij}^{n+1} \tag{9}$$

In Equation (9), σ_{ij}^{n+1} stands for nominal Cauchy stress at new increment whereas $\tilde{\sigma}_{ij}^{n+1}$ represents effective stress at new increment. An element is considered fully failed when $D \geq D_{del} = 0.95$, where all stress components are reduced to threshold value, representing physically separated or fracture state of computational specimen.

3.2. Multiaxial sequential loading simulation

The material performance under a complex loading scenario and its yield surface evolution comprising non-proportional loading is one of the highly demanding problems in computational plasticity. Classical yield criteria (Von Mises, Hill) assume the yield locus remains centred at the stress-space origin and simply expands isotropically. However, in reality successive plastic probes shift, distort, and rotate the elastic domain through kinematic hardening. Capturing anisotropic yield behaviour within the built-in constitutive models of commercial finite element software is not adequate for general quadratic criteria such as the Szczepiński model. Therefore, capturing that behaviour in a finite element simulation requires a user-defined material subroutine (UMAT) written at the constitutive level, combined with a carefully controlled experimental-numerical probing strategy. This section broadly describes the mathematical formulations for UMAT developed for this study, its numerical implementation within ABAQUS, and the iterative probing methodology used to extract yield points from simulation output. All 17 simulated probing paths developed in this section are validated quantitatively against the experimental yield points with angular accuracy assessed against α_{exp} and stress accuracy assessed against σ_{exp} and τ_{exp}. The constitutive parameters used in the UMAT comprising the five Szczepiński yield-surface coefficients and Armstrong–Frederick kinematic hardening constants were calibrated by inverse modelling against experimentally measured sequential probing data using a Levenberg–Marquardt nonlinear least-squares optimizer, as elaborated in Sections 3.2.1 and 3.2.7.

3.2.1. The Szczepiński yield criterion

The Szczepiński yield criterion defined in the (σ, τ) stress space of axial normal stress and shear stress is a general quadratic function [5]:

$$f(\sigma,\tau) = A_s\sigma^2 + 2B_s\sigma\cdot\tau + C_s\tau^2 + 2D_s\sigma + 2F_s\tau - 1 = 0 \tag{10}$$

In Equation (10), A_s, B_s, C_s, D_s, F_s are five material constants that fully define the shape, size, orientation, and centre position of the yield ellipse. It can be noted here that the form is consciously general: when $B_s = D_s = F_s = 0$ and $A_s = C_s = \frac{1}{\sigma_Y^2}$, it reduces to the Von Mises criterion. The linear terms D_s and F_s shift the ellipse centre away from the stress-space origin, which is exactly what physically causes the kinematic amplification, while the coupling term B_s allows for ellipse inclination. A MATLAB program has been developed to obtain the best fit of all 17 experimental yield surfaces using a least-squares optimisation procedure.

The goodness of fit achieved is 99% with RMS error of 0.08255 and maximum absolute deviation of 0.1123 which demonstrate the excellent fit with experimental points. The five constants calibrated for LENS-deposited Inconel 625 in its initial state are $A_s = 5.827 \times 10^{-6}$, $B_s = 4.147 \times 10^{-7}$, $C_s = 1.145 \times 10^{-5}$, $D_s =$ -5.025 $\times 10^{-7}$ and $F_s =$ -1.096 $\times 10^{-4}$. The Szczepiński coefficients were calibrated using a Levenberg–Marquardt (LM) least-squares optimizer and also used for Armstrong–Frederick parameters identified in Section 3.2.7, ensuring methodological consistency across both stages of the constitutive calibration.

3.2.2. Elastic-plastic split and stress definition

The total strain increment $\Delta\boldsymbol{\varepsilon}$ is decomposed into elastic and plastic parts, as follows [12]:

$$\Delta\boldsymbol{\varepsilon} = \Delta\boldsymbol{\varepsilon}^{el} + \Delta\boldsymbol{\varepsilon}^{pl} \tag{11}$$

In Equation (11), $\Delta\boldsymbol{\varepsilon}$ represents total strain increment tensor, $\Delta\boldsymbol{\varepsilon}^{el}$ stands for elastic strain increment and $\Delta\boldsymbol{\varepsilon}^{pl}$ is plastic strain increment. An elastic predictor trial stress is computed first by using the following expression [12]:

$$\boldsymbol{\sigma}^{tr} = \boldsymbol{\sigma}^{(n)} + \mathbf{C}^{el} : \Delta\boldsymbol{\varepsilon} \tag{12}$$

In Equation (12), $\boldsymbol{\sigma}^{tr}$ is trial stress tensor, $\boldsymbol{\sigma}^{(n)}$ is stress at the end of previous increment and $\mathbf{C}^{el}$ is the isotropic elastic stiffness tensor which can be evaluated using following relation [23]:

$$C_{ij}^{el} = \lambda\delta_{ij}\delta_{kl} + \mu\left(\delta_{ik}\delta_{jl} + \delta_{il}\delta_{jk}\right) \tag{13}$$

In Equation (13), λ, μ and δ_{ij} represent material constants defined in Equation (2).

3.2.3. Yield function in shifted stress space

The Szczepiński criterion in Equation (16) is evaluated using the shifted stress evaluated by subtracting back-stress α and expressed as [5, 10]:

$$\hat{\sigma} = \sigma_{33} - \alpha_{33} \tag{14}$$

$$\hat{\tau} = \sigma_{23} - \alpha_{23} \tag{15}$$

$$f(\hat{\sigma},\hat{\tau}) = A_s\hat{\sigma}^2 + 2B_s\hat{\sigma}\cdot\hat{\tau} + C_s\hat{\tau}^2 + 2D_s\hat{\sigma} + 2F_s\hat{\tau} - 1 \tag{16}$$

In Equation 14 and 15, α is the back-stress tensor with α_{33} and α_{23} denoting its axial and shear components, respectively. If $f \leq 0$: the response is elastic, the trial stress is accepted directly and if $f > 0$: plastic flow has occurred and return mapping is performed.

3.2.4. Plastic flow rule and return mapping

For the Szczepiński quadratic yield function $f(\hat{\sigma},\hat{\tau})$, the associative flow rule is expressed as [12]:

$$\Delta\varepsilon^{pl} = \Delta\gamma\cdot\frac{\partial f}{\partial\hat{\sigma}} \tag{17}$$

In Equation (17), $\Delta\gamma$ is plastic multiplier increment and $\frac{\partial f}{\partial\sigma}$ stands for the yield surface gradient. Accordingly, the components of the yield surface outward normal gradient $\boldsymbol{g} = \frac{\partial f}{\partial\sigma}$ which defines the direction of associative plastic flow as follows [5,16]:

$$g_\sigma = \frac{\partial f}{\partial\hat{\boldsymbol{\sigma}}} = 2A_s\hat{\sigma} + 2B_s\hat{\tau} + 2D_s \tag{18}$$

$$g_\tau = \frac{\partial f}{\partial\hat{\boldsymbol{\tau}}} = 2B_s\hat{\sigma} + 2C_s\hat{\tau} + 2F_s \tag{19}$$

In Equations (18) and (19), g_σ and g_τ are the axial and shear components of the yield surface gradient g at the current stress state. These are unnormalized gradient components of the quadratic yield function which is the standard form for associative flow rules with non-circular yield surfaces. The true unit normal can be represented as:

$$\hat{n} = g/\|g\| \tag{20}$$

In Equation (20), $\|g\| = \sqrt{g_\sigma^2 + g_\tau^2}$, and is used explicitly in the Armstrong–Frederick back-stress evolution (Section 3.2.7). In the return-mapping equations, the unnormalized gradient is used directly alongside a consistently defined plastic multiplier $\Delta\gamma$ exactly as the deviatoric stress s_{ij} serves as the unnormalized flow direction in classical Von Mises return mapping.

The stress return is computed iteratively. In each Newton iteration, the stress correction is expressed as [23,29]:

$$\sigma_{33}^{new} = \sigma_{33}^{tr} - 2\mu\cdot\Delta\gamma_{tot}\cdot n_\sigma \tag{21}$$

$$\sigma_{23}^{new} = \sigma_{23}^{tr} - 2\mu\cdot\Delta\gamma_{tot}\cdot n_\tau \tag{22}$$

$$\sigma_{11}^{new} = \sigma_{22}^{new} = \sigma_{11}^{tr} - \lambda\cdot\Delta\gamma_{tot}\cdot n_\sigma \tag{23}$$

In Equations 21–23, λ is the first Lamé constant, $\Delta\gamma_{tot}$ is total accumulated plastic multiplier across all Newton–Raphson iterations and σ_{33}^{tr}, σ_{23}^{tr} are trial axial and shear stresses. Notably, above equations represent the cumulative stress correction after convergence and within each Newton iteration, incremental corrections $\Delta(\Delta\gamma)$ are applied. The plastic multiplier incremental correction in each Newton–Raphson iteration is obtained by linearising the yield function residual with respect to $\Delta\gamma$, accounting for the simultaneous evolution of stress and back-stress [29]:

$$\Delta(\Delta\gamma) = \frac{f(\hat{\sigma},\hat{\tau})}{\mathscr{H}} \tag{24}$$

In Equation (24), the total algorithmic modulus $\mathscr{H}$ is written as:

$$\mathscr{H} = (\lambda + 2\mu)g_\sigma^2 + 2\mu g_\tau^2 + C_{AF}\left(g_\sigma^2 + g_\tau^2\right) - \gamma_{AF}\frac{\alpha_\sigma g_\sigma + \alpha_\tau g_\tau}{\|g\|} \tag{25}$$

In Equation (25), the first two terms represent the elastic stiffness projection onto the yield surface gradient in the axial and shear directions respectively, consistent with the plane-stress Szczepiński formulation where the axial direction involves both Lamé constants $(\lambda + 2\mu)$ and the shear direction involves 2μ only. The third term $C_{AF}\left(g_\sigma^2 + g_\tau^2\right)$ is the linearised kinematic hardening contribution from the Armstrong–Frederick modulus, which increases the total modulus and stabilises convergence by capturing the rate at which back-stress accumulation resists further plastic flow. The fourth term $-\gamma_{AF}(\alpha\cdot g)/\|g\|$ is the nonlinear dynamic recovery projection, which reduces the effective modulus when the back-stress is aligned with the current flow direction correctly capturing the saturation behaviour of the Armstrong–Frederick rule. This complete expression of $\mathscr{H}$ is the one implemented in the UMAT subroutine and is the correct denominator for the Newton–Raphson linearisation of the combined Szczepiński–Armstrong–Frederick return-mapping problem.

It is worth clarifying the relationship between the yield surface gradient components g_σ, g_τ and the unit normal $\hat{n}$ used in the Armstrong–Frederick update. In the stress-return equations (21)–(23) and PEEQ update equations (30)–(33), the unnormalized gradient g is used directly which is the standard and correct form of the associative flow rule for a quadratic yield function, where the plastic multiplier $\Delta\gamma$ is defined consistently with the unnormalized gradient. In the Armstrong–Frederick back-stress evolution (Equation (34)), the unit normal $\hat{n} = g/\|g\|$ is used which is also correct, because the AF rule physically requires the direction of plastic flow (a pure direction vector, magnitude $= 1$), not the gradient magnitude. The two conventions are therefore not inconsistent as they serve different physical roles in the same algorithm. The complete return-mapping procedure converges in a mean of 3–5 N–Raphson iterations per increment across all 17 probing paths, confirmed by the tolerance $|f| \leq 10^{-8}$ enforced in the UMAT.

It is important to distinguish this implementation detail from standard practice in radially symmetric yield criteria. For the J_2/Von Mises criterion, the return-mapping direction is fixed throughout iteration, and many implementations use a closed-form single-step solution with no Newton iteration at all [29,30]. In such cases, there is no practical distinction between a local Newton correction and the total plastic multiplier. For the Szczepiński quadratic surface, the gradient direction depends on the current shifted stress and therefore changes at every Newton iteration. Convergence typically requires 3–5 iterations per increment. Each local correction, $\Delta\gamma_i$ satisfies the yield residual incrementally.

The physically meaningful plastic multiplier for the increment is the converged sum, $\Delta\gamma_{tot} = \sum_i \Delta\gamma_i$, applied with the gradient evaluated at the converged stress state, consistent with implicit backward-Euler return mapping theory. Utilising only the final iteration's local correction instead of the converged sum systematically underestimates the plastic strain and equivalent plastic strain increment because the 0.01 offset yield criterion used in this numerical methodology is evaluated directly against the accumulated PEEQ state variable. This underestimation would propagate into an incorrect identification of the yield point for every one of the 17 sequential paths. This is worth highlighting here because it represents a specific and reproducible hazard for anisotropic, non-radially-symmetric return mapping, not because summation over Newton iterations is itself a new numerical concept.

3.2.5. Convexity and thermodynamic admissibility of associated flow

The use of associated flow with a yield function containing linear stress terms has a clear precedent in the anisotropic plasticity literature [31]. Szczepiński [5] proposed a general quadratic yield condition for metals displaying the Bauschinger effect in which additional linear coefficients were introduced alongside the quadratic anisotropy terms. These linear coefficients broke the tension-compression symmetry of the yield surface, thereby capturing the reduced yield strength observed after load reversal. Associated plastic strain increments were obtained directly from this yield function, with no modification to the normality rule. The planar five-constant Szczepiński form adopted in the present work follows the same structure. The linear coefficients D_s and F_s perform the equivalent role. Convexity of the present yield function follows from the Hessian of its quadratic part, expressed as:

$$Q = \begin{bmatrix} A_s & B_s \\ B_s & C_s \end{bmatrix} \tag{26}$$

In Equation (26), Q is the Hessian matrix of the quadratic part of the Szczepiński yield function. The surface is convex if and only if Q is positive definite. The linear terms D_s and F_s translate the ellipse centre in stress space. They do not appear in Q and leave the curvature unchanged. Convexity is therefore independent of the back-stress translation applied during sequential probing. For the calibrated LENS-deposited IN625 constants provided in Section 3.2.1, the eigenvalues of Q are:

$$\kappa_{1,2} = \frac{(A_s + C_s) \pm \sqrt{(A_s - C_s)^2 + 4B_s^2}}{2} = 5.797 \times 10^{-6} \text{ and } 1.148 \times 10^{-5} \quad (27)$$

Both eigenvalues are strictly positive. The determinant provides an independent check as follows:

$$\det(Q) = A_s C_s - B_s^2 = 6.65 \times 10^{-11} > 0 \quad (28)$$

Since $A_s > 0$ and $\det(Q) > 0$, Q is positive definite. The calibrated yield locus forms a strictly convex ellipse across the full 360° stress domain. This convexity result allows Drucker's stability postulate [32] to be invoked directly. For a convex yield surface, the associative normality rule assures:

$$(\sigma - \alpha) : d\varepsilon^{pl} \geq 0 \text{ [for any sequential stress path]} \quad (29)$$

This condition ensures stability of the plastic response and consistency with the second law of thermodynamics. Since the linear terms D_s and F_s only translate the surface, this property is preserved identically as the yield locus shifts under the evolving Armstrong–Frederick back-stress. Thermodynamic admissibility of the associated flow assumption is therefore maintained throughout the 17 paths sequential probing history.

3.2.6. Equivalent plastic strain (PEEQ) update

The plastic strain increments assuming incompressibility are [31]:

$$\Delta\varepsilon_{33}^{pl} = \Delta\gamma_{tot} \cdot n_\sigma \quad (30)$$

$$\Delta\varepsilon_{23}^{pl} = \Delta\gamma_{tot} \cdot n_\tau \quad (31)$$

$$\Delta\varepsilon_{11}^{pl} = \Delta\varepsilon_{22}^{pl} = -\frac{1}{2}\Delta\varepsilon_{33}^{pl} \quad (32)$$

Notably, all other plastic strain components $\left(\Delta\varepsilon_{12}^{pl} \text{ and } \Delta\varepsilon_{13}^{pl}\right)$ are zero in the plane-stress Szczepiński formulation. Furthermore, the Von Mises equivalent plastic strain increment is governed by Ref. [31]:

$$\Delta\bar{\varepsilon}^{pl} = \sqrt{\frac{2}{3}\left[\left(\Delta\varepsilon_{11}^{pl}\right)^2 + \left(\Delta\varepsilon_{22}^{pl}\right)^2 + \left(\Delta\varepsilon_{33}^{pl}\right)^2 + 2\left(\Delta\varepsilon_{23}^{pl}\right)^2\right]} \quad (33)$$

The cumulative plastic strain limit is updated as $\bar{\varepsilon}_{new}^{pl} = \bar{\varepsilon}_{old}^{pl} + \Delta\bar{\varepsilon}^{pl}$ and stored in user defined state variable in subroutine. The factor 2/3 ensures energy-conjugacy and the factor 2 on the shear term accounts for engineering shear strain convention. A positive inner product signals continued loading; negative signals elastic unloading or reverse loading.

3.2.7. Armstrong–Frederick evolution law

The back-stress tensor α evolves according to the Armstrong–-Frederick nonlinear kinematic hardening rule [11]:

$$\dot{\alpha} = C_{AF}(\sigma - \alpha)\dot{\bar{\varepsilon}}^{pl} - \gamma_{AF}\, \alpha\, \dot{\bar{\varepsilon}}^{pl} \quad (34)$$

In Equation (34), α is the back-stress tensor, whose components α_{33} and α_{23} represent the kinematic shift of the yield surface centre in the axial and shear directions, respectively. C_{AF} is the kinematic hardening modulus controlling the rate of back-stress accumulation during forward plastic loading and γ_{AF} is the dynamic recovery coefficient that governs saturation and directional decay of the back-stress.

Additionally, the first term $C_{AF}(\sigma - \alpha)\dot{\bar{\varepsilon}}^{pl}$ drives the yield surface to translate in stress space, capturing the Bauschinger effect under sequential loading. The second term $\gamma_{AF}\, \alpha\, \dot{\bar{\varepsilon}}^{pl}$ is the nonlinear recall term which opposes unrestricted back-stress growth and drives the back-stress to saturation, $\alpha_{sat} = (C_{AF} / \gamma_{AF})n$, enabling simulation of yield surface rotation under the non-proportional sequential paths. The six independent components of the symmetric back-stress tensor are stored in the developed subroutine and updated at each converged Newton–Raphson increment via implicit Euler integration rule.

3.2.8. Calibration of Armstrong–Frederick parameters

The two Armstrong–Frederick constants, C_{AF} and γ_{AF}, governing the rate of back-stress accumulation and its dynamic recovery, respectively, were identified by inverse modelling against the sequential single-specimen probing dataset described in Section 2, rather than from an independent cyclic loading test. The identification was performed using Levenberg–Marquardt nonlinear least-squares optimizer implemented in MATLAB, consistent with the Szczepiński yield surface fitting method described in Section 3.2.1. The calibration was carried out in two sequential stages to separately resolve the linear hardening and saturation behaviour of the Armstrong–Frederick rule. In Stage 1, Paths P1–P2 were used, where the low accumulated plastic strain renders the dynamic recovery term negligible, allowing C_{AF} to be isolated from the initial rate of back-stress accumulation. In Stage 2, Paths P5–P13 were used, corresponding to the regime in which the back-stress trajectory approaches saturation, $\alpha_{sat} = (C_{AF} / \gamma_{AF})$, enabling identification of C_{AF} and γ_{AF} held from Stage 1. The optimizer minimized the combined sum of squared residuals between simulated and experimental axial and shear stress components across all 17 sequential paths.

The final calibrated values are $C_{AF} = 52{,}000$ MPa and $\gamma_{AF} = 185$, corresponding to a saturation back-stress of $\alpha_{sat} = 281$ MPa and a final objective function value (Sum of Squared Errors, SSE) of 0.083. These values were supplied to the UMAT and were held fixed for all forward simulations of the 17 sequential probing paths. This calibration produced a mean absolute angular error of 0.86°, a mean absolute axial stress deviation of 11.4 MPa, and a mean absolute shear stress deviation of 12.5 MPa.

3.2.9. Consistent tangent modulus

For quadratic convergence of the global Newton-Raphson iterations, the consistent tangent D^{ep} is assembled as [29]:

$$D_{ij}^{ep} = C_{ij}^{el} - \frac{2\mu}{n_\sigma^2 + n_\tau^2}\left(n_\sigma C_{i3}^{el} + n_\tau C_{i6}^{el}\right)\left(n_\sigma C_{3j}^{el} + n_\tau C_{6j}^{el}\right) \quad (35)$$

In Equation (35), D_{ij}^{ep} is the consistent elastic–plastic tangent modulus, C_{ij}^{el} is the elastic stiffness tensor and n_σ, n_τ are the yield surface normal components. C_{i3}^{el} and C_{i6}^{el} denote columns of the elastic stiffness corresponding to axial and shear directions in Voigt notation. The factor $\frac{2\mu}{n_\sigma^2 + n_\tau^2}$ represents the plastic compliance in the active stress directions. Returning towards D^{ep} instead of C^{el} ensures true quadratic convergence of the global equilibrium solver.

3.3. Probing methodology: sequential path-by-path strategy

The sequential probing strategy mirrors the Dubey et al. [13,14] experimental protocol, as explained in section 2 in which 17 radial loading paths are applied one after another on the same virtual specimen. Between each path, the specimen is fully unloaded via a force-controlled ramp to zero. Each path induces a PEEQ increment of 0.0001, so the cumulative PEEQ after path k is $k \times 0.0001$.

For each path k, the goal is to find the boundary condition (BC) set $(U3, UR3)$ axial displacement and final rotation that drives the simulation to yield in the correct stress direction, matching the experimental angle $\alpha_{exp,k} = \arctan 2(\tau_{exp}, \sigma_{exp})$.

3.3.1. The 5-step ellipse procedure

Given a target stress point (σ, τ) on the Szczepiński ellipse, the yield surface radius at that angle is computed analytically. Defining $\cos\alpha$ and $\sin\alpha$ from the loading angle, the quadratic form collapses to a scalar equations [5]:

$$A_c = A_s \cos^2\alpha + 2B_s \cos\alpha \sin\alpha + C_s \sin^2\alpha \quad (36)$$

$$B_c = 2D_s \cos\alpha + 2F_s \sin\alpha \quad (37)$$

$$r_{ell} = \frac{-B_c + \sqrt{B_c^2 + 4A_c}}{2A_c} \quad (38)$$

In Equations (36)–(38), α is probing angle in the (σ, τ) stress plane, $\alpha = \mathrm{atan}\,2(\tau, \sigma)$, A_c is angular projection of quadratic Szczepiński coefficients, B_c is angular projection of linear Szczepiński coefficients and r_{ell} is Szczepiński locus radius at angle α. The yield point coordinates are then: $\sigma_Y = r_{ell} \cos\alpha$, $\tau_Y = r_{ell} \sin\alpha$.

3.3.2. Two-step angle correction

In practise, each prior probing path deposits a small increment of equivalent plastic strain that physically shifts the yield surface in stress space. During modelling, this is represented through the Armstrong--Frederick back-stress update, which produces a progressive rotation of the elastic domain that causes the displacement-controlled boundary condition to overshoot or undershoot the experimentally realised target angle α_{exp}. An equivalent angular drift is independently confirmed by the experimental data in Table 4, where α_{exp} deviates from the nominal ideal direction by up to 7.9° at P15, with a mean absolute deviation of 4.1° across the 17 paths. The following two-step correction procedure addresses this discrepancy numerically. A two-step iterative correction was therefore implemented:

Step 1 Apply boundary condition along $\alpha_{BC} = \alpha_{exp}$. After successful completion of simulation, extract reaction force and moment at targeted plastic strain limit and compute $\alpha_{S1,sim}$ and angle error by using following relation:

$$\Delta\alpha_{S1} = \alpha_{S1,sim} - \alpha_{exp} \quad (39)$$

Step 2 **(if $|\Delta\alpha_{S1}| > 1.5°$):** Apply corrected boundary conditions along:

$$\alpha_{BC,S2} = \alpha_{exp} - \Delta\alpha_{S1} \quad (40)$$

In Equations (39) and (40), α_{exp} is experimental probing angle, $\alpha_{S1,\mathrm{sim}}$ is simulated stress angle after Run 1 (uncorrected BCs), $\Delta\alpha_{S1}$ is angular overshoot in Run 1 and $\alpha_{BC,S2}$ is corrected boundary condition angle for Run 2. If $|\Delta\alpha_{S2}| \leq 1.5°$ then only acceptable for converged value of yield surface. The correction exploits the approximately linear relationship between boundary condition direction and stress direction, offsetting the boundary condition by exactly the overshoot angle to land at the experimental target.

4. Results and discussion

4.1. Tensile fracture simulation using VUMAT

The constitutive material constants were calibrated directly against the experimentally measured true stress vs. plastic strain curve and validated against the experimentally observed fracture morphology of LENS-deposited IN625. LENS-deposited IN625 alloy exhibits a complex, nonlinear constitutive response characterised by a pronounced strain-hardening plateau followed by a triaxiality-dependent post-necking (after ultimate tensile strength) softening behaviour. Such characteristics cannot be adequately reproduced by the built-in damage models in Abaqus/Explicit module. A user-defined subroutine VUMAT was therefore implemented to incorporate a piecewise-linear isotropic hardening law calibrated directly against experimentally measured true stress vs. true plastic strain data, coupled with a triaxiality-dependent ductile damage initiation criterion. This combination physically accounts for the stress-state sensitivity of void nucleation and coalescence at LENS-deposited inter-layer interfaces.

Since damage evolution and post-peak softening are inherently mesh-sensitive in the absence of regularization, the present damage model incorporates a Hillerborg-type fracture energy regularization in which the local softening slope is scaled by the element characteristic length, $h_{loc} = \sigma_y \cdot L_{char}/G_f$, with fracture energy $G_f = 50$ N/mm calibrated for IN625. This confirms the energy dissipated during softening remains independent of element size. To verify convergence for the present geometry, a mesh sensitivity study was conducted using three mesh sizes, benchmarked against the mesh adopted for all production simulations.

Table 2 summarises the results, with deviation reported relative to the adopted 6000 element mesh size.

As shown from Table 2, both the coarser and finer meshes deviate from the adopted 6000 element mesh by less than 1% (−0.66% and +0.53%, respectively), confirming that the selected mesh density lies within a converged, discretization-insensitive regime for the predicted UTS value. This convergence behaviour verifies that the fracture-energy regularization embedded in the VUMAT effectively controls mesh sensitivity in the damage-softening regime. The 6000 element mesh was therefore adopted for all reported tensile damage simulations, providing converged accuracy at an effective computational cost.

Fig. 2 illustrates the engineering stress vs. strain response reproduced by the VUMAT subroutine superimposed on the experimental curve, with four different representative deformation stages as plastic strain progresses. As visualised, the numerically predicted response demonstrates close agreement with the experimental data across the complete deformation range. The VUMAT reproduces the initial elastic modulus, the gradual yielding transition, and the extended strain-hardening slope, achieving tensile strength prediction within ±3% of the experimental value in the hardening regime and within ±5% in the post-necking softening regime. The latter tolerance is consistent with the build-direction variability typically observed in LENS-deposited alloys due to inter-layer porosity gradients and thermally induced dislocation density fluctuations [13–15,33]. Four distinct computational deformation stages visible in Fig. 2 reflect the initial uniform gauge state, the uniformly elongated gauge at diffuse necking onset, where the plastic deformation remains stable throughout the cross-section, the localised necked profile at concentrated necking and the final fractured state, corresponding to complete tensile rupture at $D \geq 0.95$.

Fig. 3 presents a spatial comparison between the experimentally observed cup-cone fracture morphology and the VUMAT-predicted damage localisation contour at the rupture stage. The experimental fracture surface displays the two morphologically distinct zones that are the distinct feature of ductile fracture in alloys. These two zones comprise a visible central flat fibrous region dominated by void coalescence under triaxial tension and an outer inclined shear lip where the fracture plane rotates approximately 45° relative to the loading axis. As visualised from Fig. 3(a) and (b), the developed VUMAT reproduces both zones quantitatively. At the specimen periphery, the stress triaxiality drops to $\eta \in [0.3, 0.6]$, transitioning the dominant failure mechanism from triaxial void growth to shear band driven voids. This resulted in the inclined shear lip whose spatial extent and angular inclination matches the experimental fracture surface. The predicted fracture plane location along the gauge length, its inclination angle relative to the loading axis, and the relative proportions of the flat fibrous and shear lip zones are all reproduced within the dimensional tolerances observable from the experimental fractured specimen image shown in Fig. 3(b). It can be highlighted here that the elastic constants calibrated at this stage are not only specific to the damage model but also define the isotropic elastic stiffness tensor used identically in Section 4.2. No separate elastic

Table 2
Mesh convergence study for the tensile damage simulation.

Mesh Size	No. of Elements	No. of Nodes	σ_{UTS} (MPa)	% Deviation
Coarse	4200	9745	873.8	−0.66
Medium	6000	12121	879.6	0.0
Fine	6800	13736	884.3	+0.53

Table 3
Mesh convergence study for representative sequential loading paths P1, P5, and P9.

Path	Mesh	Through thickness Elements	No. of Elements	No. of Nodes	σ_{sim} (MPa)	τ_{sim} (MPa)	r_{sim} (MPa)	%Dev. vs M4
P1	M2	2	262	442	418.04	0	418.04	+0.93
	M4	4	524	1054	414.21	0	414.21	-
	M8	8	1048	2147	412.47	0	412.47	−0.42
P5	M2	2	262	442	−23.76	339.18	340.01	+2.24
	M4	4	524	1054	−23.24	331.78	332.59	-
	M8	8	1048	2147	−23.05	328.98	329.59	−0.84
P9	M2	2	262	442	−414.37	−4.17	414.39	+0.90
	M4	4	524	1054	−410.68	−4.14	410.70	-
	M8	8	1048	2147	−409.13	−4.12	409.15	−0.38

Table 4
Experimental probing path angles and yield points for all 17 sequential biaxial loading paths of LENS-deposited Inconel 625.

Path	Ideal α	α_{exp} (°)	σ_{exp} (MPa)	τ_{exp} (MPa)	r_{exp} (MPa)
P1	0°	2.970	400.964	20.832	401.505
P2	30°	27.008	335.008	170.751	376.014
P3	45°	40.330	276.254	234.528	362.381
P4	60°	56.400	181.495	273.167	327.964
P5	90°	93.929	−19.945	290.367	291.051
P6	120°	126.881	−199.178	265.460	331.875
P7	135°	141.723	−296.915	234.300	378.226
P8	150°	155.350	−380.273	174.503	418.400
P9	−180°	−179.039	−404.323	−6.785	404.380
P10	−150°	−152.809	−290.812	−149.401	326.944
P11	−135°	−137.639	−251.867	−229.669	340.859
P12	−120°	−122.241	−171.968	−272.648	322.351
P13	−90°	−89.201	3.886	−278.505	278.532
P14	−60°	−54.794	174.857	−247.816	303.295
P15	−45°	−37.077	287.631	−217.351	360.518
P16	−30°	−22.655	376.612	−157.189	408.099
P17	0°	1.943	400.823	13.596	401.054

calibration is performed for the multiaxial UMAT.

4.2. Biaxial sequential loading simulation

This section deals with the advanced finite element simulation that replicates all 17 sequential tension/compression–torsion probing paths of a single tubular specimen under combined displacement and rotation controlled loading, using a user defined Szczepiński-UMAT with iterative angular boundary condition correction, for AM nickel-base alloys. The Szczepiński-UMAT framework presented in this section is validated against the 17 experimental yield points with quantitative accuracy metrics reported path-by-path.

4.2.1. Specimen geometry and finite element model

To isolate the constitutive response from grip-induced end effects and to maintain a computationally efficient model, only the parallel gauge section of the experimentally tested tubular specimen is retained in the finite element model as shown in Fig. 4.

The gauge section is a hollow cylinder with outer radius $R_o = 5.2$ mm, inner radius $R_i = 4.2$ mm and gauge length $L = 20$ mm resulting in wall thickness, $t = 1.0$ mm, giving a wall-to-radius (t/R_o) ratio of 0.192, close to the conventional thin-wall guideline of 0.2. As mentioned earlier, Paths P1 and P17 sequential probe are near-pure tension regimes. Both originate from the same virgin material state and henceforth, use the same elastic constants calibrated in Section 4.1.Since this

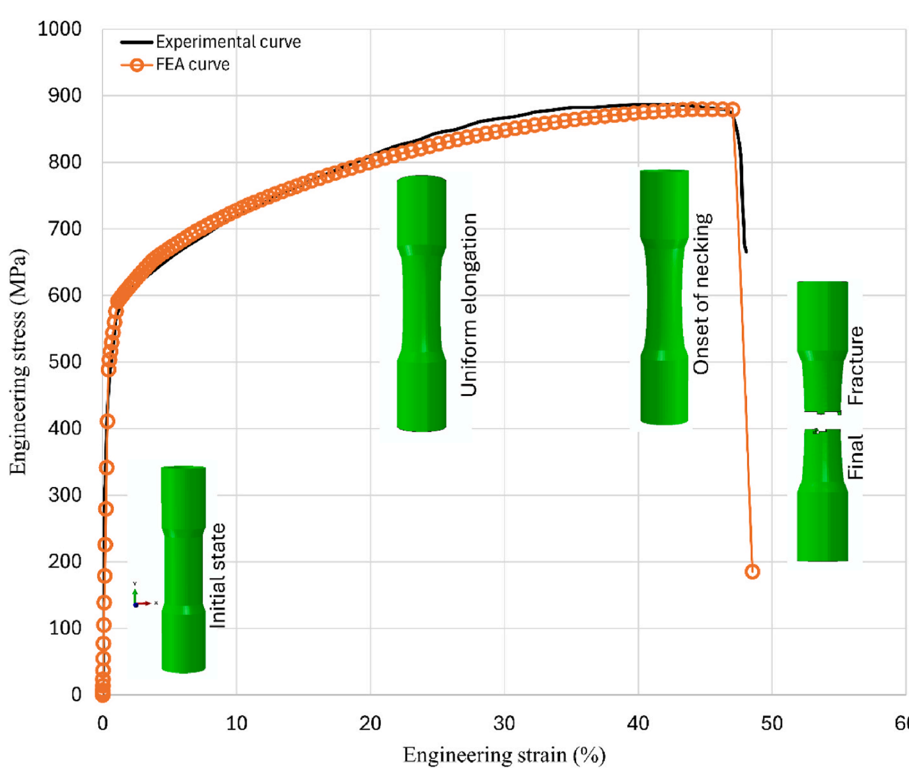

Fig. 2. Experiment and simulated superimposed tensile curve for LENS-deposited Inconel 625 alloy with different representative deformation stages.

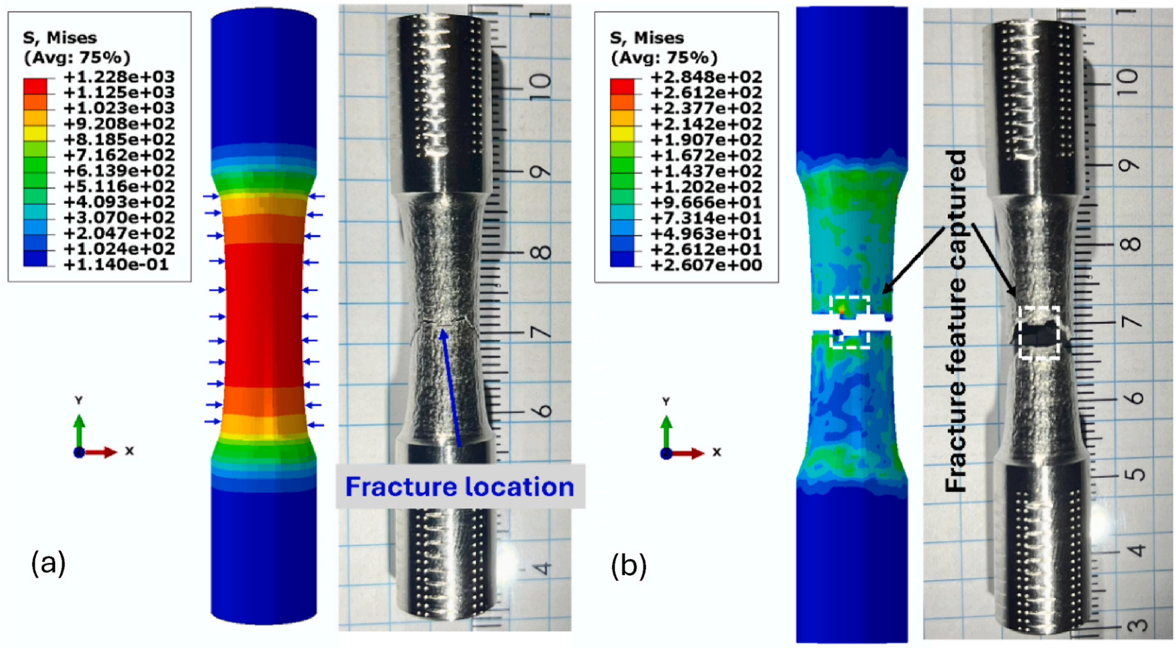

Fig. 3. Experimentally and simulated (a) cup-cone fracture morphology at the onset of rupture and (b) VUMAT-predicted damage localisation contour for LENS-deposited IN625 alloy.

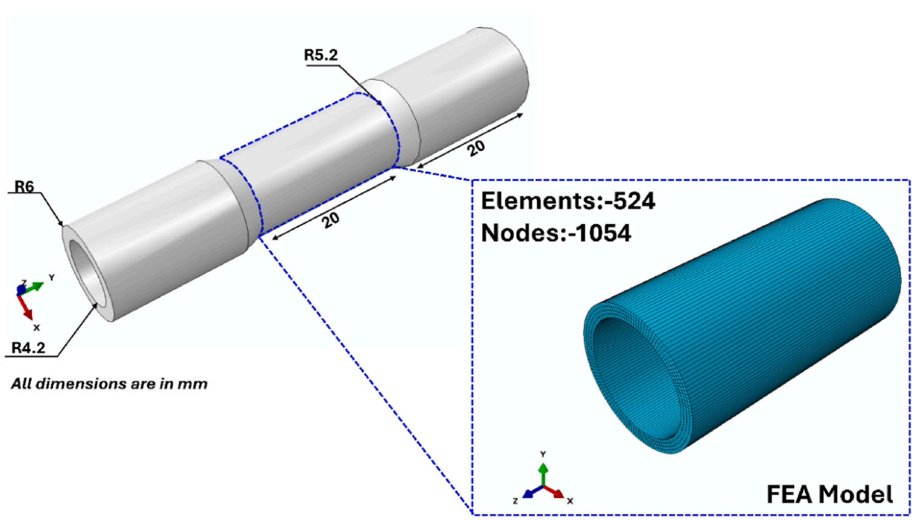

Fig. 4. Selection of computational domain form tubular thin walled hollow cylinder used for sequential bi-axial loading simulation.

ratio is near the threshold, through-thickness stress uniformity was not assumed but explicitly verified via the mesh convergence and gradient analysis presented in Section 4.2.2. The section is discretised using 8-node linear brick, reduced-integration continuum solid elements (C3D8R) with ABAQUS default enhanced hourglass control, using four elements through the wall thickness and producing a structured mesh of 524 elements. This mesh density was confirmed as adequate through the convergence study detailed in Section 4.2.2.

4.2.2. Mesh convergence study

The present simulations follow a sequential single-specimen probing method in which each loading path is applied only after the specimen has been fully unloaded following all preceding paths. Consequently, simulating n^{th} path requires the model to first replay paths 1 through $(n-1)$ to correctly reconstruct the accumulated Armstrong–Frederick back-stress state, so the computational cost of each successive path increases cumulatively along the sequence. A full mesh convergence study repeated across all 17 sequential paths at multiple mesh densities would therefore require re-simulating the entire cumulative loading history multiple times over, at a computational cost disproportionate to the verification objective. To address mesh adequacy efficiently three representative paths were selected to span the full range of accumulated loading history and fundamental stress state: P1 (first path, no prior loading history, near-pure tension), P5 (after four prior probes, near-pure torsion where the stress state becomes most sensitive to through-thickness discretization), and P9 (after eight prior probes near-pure compression, near the sequence midpoint). For each path, three through-thickness mesh densities of 2 elements (M2), 4 elements as adopted in this study (M4), and 8 elements (M8) were evaluated with in-plane discretization kept fixed.

For each mesh density the axial and torsional shear stress components at yield were computed from the global reaction force (RF3) and reaction moment (RM3) at the reference point, corresponding to the cumulative equivalent plastic strain reaching the 0.01% offset limit. This reaction-based approach converts the global force and moment output directly into nominal axial and shear stress via the thin-wall tube relations, independent of any local point-wise stress extraction. To additionally assess the influence of through-thickness discretization on the internal stress field, axial and shear stress values were also examined at the innermost and outermost through-thickness integration points at the mid-gauge cross-section for the torsion-dominated path P5, quantifying the local gradient captured by each mesh density without altering the global reaction-based yield stress definition used for all reported results. Table 3 summarises these results.

The results confirm that the adopted 4-element (M4) mesh lies within the converged, discretization-insensitive regime for the reaction-based yield stress. Refinement to M8 changes the yield radius by less than 1% for all three paths (0.42% for P1, 0.84% for P5, 0.38% for P9), while coarsening to M2 produces a deviation of up to 2.24% at the torsion-dominated path P5. A local through-thickness shear stress gradient is present at P5 and increases modestly with mesh refinement, as physically expected for a tube with (t/R_o) close to the thin-wall limit. Quantitatively, the shear stress varies by approximately 24% between the inner and outer wall radii under torsion-dominated loading. This is consistent with the elastic through-wall gradient predicted by Saint-Venant torsion theory for the present $(t/R_o) = 0.192$ geometry. However, this internal gradient does not influence the reaction-based yield stress values reported in the manuscript, since RF3 and RM3 are global equilibrium quantities integrated over the reference-point coupling rather than local stress samples. Since mesh sensitivity of the reported yield stress arises from spatial discretization of the global reaction output rather than from the magnitude of accumulated back-stress history, convergence demonstrated at these three representative history depths is considered representative of mesh behaviour throughout the full 17 paths sequences. The 524-element mesh was therefore retained as the optimal choice, balancing converged accuracy against the computational cost of the cumulative path replay required at each stage of the sequence.

Furthermore, the mesh topology, element type, and reference point coupling remain identical across all 17 sequential loading paths; only the magnitudes for axial deformation and rotational fields are updated path-by-path, with a cumulative equivalent plastic strain increment of $\Delta\bar{\varepsilon}^p = 1 \times 10^{-4}$ per path serving as the consistent yield offset criterion, directly replicating the 0.01% plastic strain definition adopted in the experimental practices. The top surface of the gauge section is kinematically coupled to a central reference point, through which the prescribed axial displacement U_3 and torsional rotation UR_3 are applied simultaneously in a displacement-controlled manner to impose the desired (σ, τ) stress ratio at the target probing angle α_{exp}. The bottom surface is fully constrained, replicating the fixed grip condition of the experimental boundary condition. The initial boundary condition pair for each path is computed directly from the experimental yield stresses as $U_3 = \frac{\sigma_{exp}L}{E}$ and $UR_3 = \frac{\tau_{exp}L}{G \cdot R_o}$, establishing Run 1 with $\alpha_{BC} = \alpha_{exp}$. However, the elastic anisotropy of the Szczepiński surface creates a compliance coupling between the axial and shear directions that prevents a purely displacement-controlled loading from reproducing the target stress ratio α_{exp} accurately. The two-step iterative boundary condition discussed in Section 3.3.2 is therefore applied and quantified in Table 5 to drive the simulated stress angle to within the acceptance criterion $|\Delta\alpha| \le 1.5^\circ$ for each path. Having established the geometry and kinematic framework, the next section presents the experimental yield data that constitutes the primary benchmark for all subsequent comparisons.

4.2.3. Experimental yield locus and different path maps

Table 4 summarises the experimental probing path data for all 17 sequential loading paths. The ideal α column lists the nominal target probing direction spanning 0° to 360°, sampled in 15° increments between P2–P3, P3–P4, P6–P7, P7–P8, P10–P11, P11–P12, P14–P15, and P15–P16 paths, whereas in 30° increments at P1–P2, P4–P5, P5–P6, P8–P9, P9–P10, P12–P13, P13–P14, and P16–P17 paths, reflecting the experimental strategy of sampling more densely in the near-tensile and oblique sectors where the yield locus curvature is higher, and more coarsely across the near-pure shear, compressive–shear, and pure compression transition sectors.

Notably, the actual experimental stress angle α_{exp} deviates systematically from the nominal ideal target across successive paths, with deviations ranging from a minimum of 0.8° at P13 to a maximum of 7.9° at P15, and a mean absolute deviation of 4.1° across all 17 paths. It is important to emphasize that these deviations do not represent an experimental error or a misfit of the Szczepiński ellipse. The α_{exp} values listed in Table 4 are the true experimentally realised stress angles the actual directions in the (σ, τ) plane along which yielding occurred in each probing path, computed directly from the measured reaction force and torque at the 0.01% plastic strain (PEEQ) offset as $\alpha_{exp} = \arctan(\tau_{exp} / \sigma_{exp})$.

Furthermore, the departure from the nominal ideal directions is a directly measured physical observation. The realised stress ratio in the gauge section consistently differs from the nominally prescribed displacement-controlled boundary condition. This discrepancy evolves path-by-path as the sequential probing cycle progresses. Distinctly, two physical mechanisms contribute to this observed angular drift. The first one is the elastic compliance coupling inherent to displacement-

Table 5
Simulated yield point data for all 17 paths illustrating converged angle α_{sim}, residual $\Delta\alpha$, actual simulated stresses σ_{sim}/τ_{sim}, Szczepiński locus radius r_{ell}, and ellipse-projected coordinates σ_Y/τ_Y.

α_{sim} (°)	$\Delta\alpha$ (°)	σ_{sim} (MPa)	τ_{sim} (MPa)	r_{ell} (MPa)	σ_Y (MPa)	τ_Y (MPa)
0.000	−2.970	414.205	0.000	414.357	414.357	0.000
26.264	−0.744	347.327	171.390	377.996	338.973	167.268
40.356	+0.026	278.851	236.953	349.489	266.323	226.307
56.383	−0.017	191.597	288.190	323.666	179.195	269.535
94.007	+0.078	−23.243	331.781	306.357	−21.410	305.608
126.259	−0.622	−216.382	295.011	341.513	−201.983	275.380
142.801	+1.078	−312.074	236.864	374.442	−298.260	226.380
156.825	+1.475	−376.868	161.333	402.064	−369.620	158.230
−179.423	−0.384	−410.684	−4.136	413.679	−413.658	−4.166
−153.798	−0.989	−322.795	−158.848	364.661	−327.189	−161.011
−137.743	−0.104	−244.294	−221.953	329.085	−243.569	−221.294
−120.973	+1.268	−158.989	−264.884	302.164	−155.504	−259.078
−87.862	+1.339	11.096	−297.240	286.552	10.690	−286.352
−53.840	+0.954	197.383	−270.087	321.963	189.971	−259.944
−36.317	+0.760	299.458	−220.110	358.889	289.176	−212.553
−21.461	+1.194	372.294	−146.355	392.247	365.052	−143.508
1.399	−0.544	413.359	10.098	413.978	413.854	10.110

controlled biaxial loading, whereby the prescribed displacement-to-rotation ratio at the specimen boundary does not map exactly onto the target stress ratio at the gauge cross-section. The second mechanism is a progressive path-by-path shift of the yield surface in stress space, as each preceding probe deposits a small increment of equivalent plastic strain that incrementally modifies the elastic domain seen by the next probe. The Armstrong–Frederick nonlinear kinematic hardening model adopted in this work provides a constitutive interpretation of second mechanism. It represents the yield surface shift through the evolution of a tensorial back-stress variable. It is emphasised, however, that the back-stress is a model construct which cannot be measured directly from the experimental practise. Its application in present work represents a model-consistent interpretation of the observed angular drift, not an independently verified causal mechanism.

Furthermore, this experimentally observed angular drift between the nominal ideal direction and the realised stress angle α_{exp} is the directly measured quantity that necessitates the two-step boundary-condition correction procedure described in Section 3.3.2. The correction is applied to the simulation to ensure the virtual probe reaches the same stress direction as the experiment regardless of the physical mechanism responsible for the drift. Its successful reduction of the simulation-to-experiment angular residual to within $\pm 1.5^{\circ}$ for 16 of 17 paths constitutes one of the principal algorithmic contributions of the present UMAT framework. The single exception, Path P1, is explicitly discussed in Section 4.2.8. It is noted that the scalar yield radius $r_{exp} = \sqrt{\sigma_{exp}^2 + \tau_{exp}^2}$ represents the Euclidean distance from the stress-space origin to each experimental yield point in the (σ, τ) plane. As listed in Table 4, r_{exp} varies from a minimum of 278.5 MPa at P13 (near-pure negative shear path) to a maximum of 418.4 MPa at P8 (compression–torsion path), a directional spread of 139.9 MPa representing 50.2% of the minimum value. It is essential to note that the physically meaningful isotropic comparator is therefore the Von Mises equivalent stress $\sigma_{VM} = \sqrt{\sigma_{exp}^2 + 3 \cdot \tau_{exp}^2}$, which remains constant at yielding for all probing directions in a truly isotropic material. Computing σ_{VM} directly from Table 4 reveals values ranging from 389.3 MPa at P10 to 506.8 MPa at P4, a directional spread of 117.5 MPa representing 30.2% of the minimum σ_{VM}. This directional variation constitutes direct and unambiguous experimental evidence that the yield threshold of LENS-deposited IN625 is genuinely direction-dependent. This anisotropy cannot be captured by the classical Von Mises criterion and provides the primary quantitative motivation for implementing the five-parameter Szczepiński anisotropic yield function in the present UMAT framework.

It is noted that the deviation of α_{exp} from the nominal Ideal α does not represent an experimental error or a fitting residual of the Szczepiński ellipse. Rather, it reflects two superimposed physical effects: the finite elastic compliance coupling of the biaxial testing machine under displacement-controlled loading, and the progressive shift of the yield surface accumulated from each preceding probing path. The α_{exp} values are the true experimentally realised stress angles, computed directly from measured reaction force and torque at the 0.01% plastic strain offset and constitute the correct reference directions for all subsequent simulation validations.

Additionally, Paths P1 and P17 both target the near-pure tensile direction and serve as the opening and closing probes of the full sequential cycle, providing an intrinsic specimen level repeatability check. The experimental yield radii are r_{exp} (P1) = 401.5 MPa and r_{exp} (P17) = 401.1 MPa, agreeing to within 0.45 MPa (0.11%) despite the cumulative equivalent plastic strain of $\Sigma \Delta \bar{\varepsilon}^p = 16 \times 10^{-4}$ introduced by the intervening 15 probing paths.

This near-identical yield response at the same stress direction after a complete 360° probing cycle confirms important features of the experimental dataset. The specimen remained mechanically stable throughout the sequential test and there is no significant isotropic hardening or progressive specimen damage accumulated beyond the controlled kinematic back-stress offset, and the experimental data are internally self-consistent. Together, these features confirm that the experimental points constitute a reliable quantitative benchmark for the subsequent numerical validation presented in Section 4.2.3 onwards.

Fig. 5 presents the polar representation in the (σ, τ) stress plane, with each point positioned at coordinates (r_{exp}, α_{exp}). The corresponding experimental paths are detailed in Table 4. This polar map provides an intuitive overview of the yield locus geometry and allows for evaluation of the initial boundary condition pairs (U_3, UR_3) for each simulation via the ellipse technique of Section 4.3.2. Any angular discrepancy in translating the experimental polar coordinates into combined displacement and rotation boundary conditions would propagate as a systematic bias in the probed direction on the yield surface. Therefore, to confirm that this propagation does not compromise the deformation condition of the model, the following section examines the uniformity of the simulated deformation field across the gauge section for representative loading combinations.

4.2.4. Verification of deformation field homogeneity

Fig. 6 illustrates the displacement magnitude contours at the yield instant for three different representative tension/compression-torsion paths that span the primary loading regimes as (a) P1 (α_{exp} is 2.97°, pure axial tension), (b) P5 (α_{exp} is 93.9°, pure torsion), and (c) P8 (α_{exp} is 155.4°, combined compression and torsion, where $r_{exp} = 418.4$ MPa the largest experimental yield radius among all 17 paths). In Fig. 6(a), the displacement contours vary monotonically along the specimen axis with circumferentially uniform iso-displacement coloured contours, confirming the absence of torsional loading and a homogeneous uniaxial axial stress state across the full wall thickness. In Fig. 6(b), the contour field exhibits a linearly increasing angular rotation from the fixed base toward the loaded end, producing the characteristic helical element distortion expected under only torsional loading. In Fig. 6(c), the superposition of axial compression and angular twist generates a spiralling deformation field whose amplitude increases toward the loaded end. The spatial uniformity of the contour bands along the gauge length confirms that the selected mesh type resolves the combined stress state without additional end-effect penetration. The thin-wall assumption is therefore validated numerically for all three representative loading paths and for all 17 loading combinations confirming the stress extraction from reaction outputs (force and moment) as the primary source of the $(\sigma_{sim}, \tau_{sim})$ yield surface reported in Table 5.

4.2.5. Axial and torsional shear stress contour plots

Fig. 7 presents contour plots of the axial (SDV12) and torsional shear (SDV15) user-defined state variables at the 0.01% equivalent plastic strain offset for four representative paths spanning (a) P1 (near-pure tension), (b) P5 (near-pure torsion), (c) P9 (near-pure compression), and (d) P13 (sequential negative shear following twelve prior probes). These constitutive state variables are reported in place of the generic isotropic Von Mises invariant computed internally by ABAQUS, because plastic flow in the present framework is governed exclusively by the anisotropic Szczepiński criterion evaluated in the shifted stress space $(\hat{\sigma}, \hat{\tau})$ space. The built-in isotropic J_2 invariant bears no direct relationship to the anisotropic yield surface driving the return-mapping algorithm and is therefore not the physically governing output in this framework.

Fig. 7(a): Contour plot of the axial stress state variable (SDV12) at the 0.01% equivalent plastic strain offset for Path P1 (near-pure tension), showing a spatially uniform value of 414.4 MPa across the gauge section.

For Path P1, Fig. 7(a) shows a fully uniform SDV12 field of 414.4 MPa, matching $\sigma_{sim} = 414.205$ MPa from Table 5 to within 0.05%, since pure axial extension ($\tau_{exp} \approx 0$) generates no through-wall shear gradient. This uniformity independently confirms the deformation field homogeneity already established in Section 4.2.3 (Fig. 6(a)) and demonstrates that the plastic multiplier accumulation scheme of Equation (23)

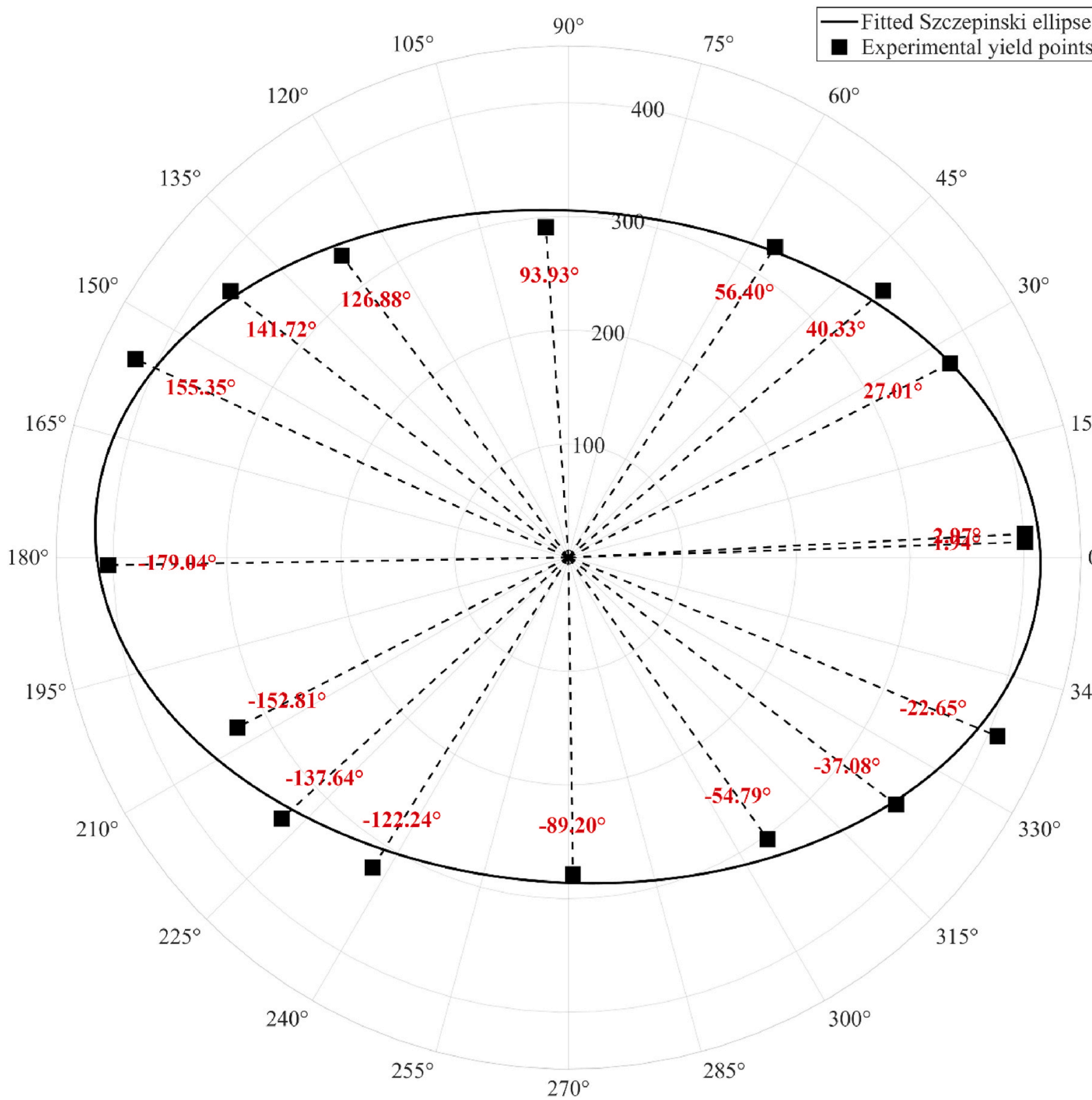

Fig. 5. Polar representation of the experimental yield locus for LENS-deposited IN625 in the biaxial (σ, τ) stress plane.

converges to a spatially constant solution under monotonic proportional loading.

For Path P5, Fig. 7(b) reflects SDV12 spanning −36.8 to −13.8 MPa whereas SDV15 spanning 283.6 to 306.2 MPa across the wall thickness, bounding $\sigma_{sim} = -23.24$ MPa and $\tau_{sim} = 331.78$ MPa listed in Table 5 within, or immediately adjacent to, the outer-surface extremum of this range. As mentioned earlier, this finite spatial spread is absent in Path P1 which is a direct exhibition of the analytically quantified through-wall shear gradient acting in combination with the near-pure-torsion loading state, in which the Szczepiński ellipse bulges furthest beyond the isotropic reference (AI(α) = 1.215, Section 4.2.10) and is therefore most sensitive to any residual angular correction. The close bound between the local SDV15 range and the section-averaged τ_{sim} confirms that the elevated shear response at P5 originates from a physically consistent, mesh-resolved stress state rather than from a localised numerical artefact.

Fig. 7(b)–(d): Contour plots of the axial (SDV12) and torsional shear (SDV15) stress state variables at the 0.01% equivalent plastic strain offset for (b) Path P5 (near-pure torsion): SDV12 ranges from −36.8 to −13.8 MPa and SDV15 ranges from 283.6 to 306.2 MPa across the wall thickness; (c) Path P9 (near-pure compression): SDV12 ranges from −413.5 to −408.4 MPa and SDV15 ranges from −29.7 to 19.6 MPa; and (d) Path P13 (sequential negative shear, following twelve prior probing paths): SDV12 ranges from 3.4 to 28.8 MPa and SDV15 ranges from −286.7 to −228.6 MPa.

For Path P9, Fig. 7(c) shows SDV12 spanning −413.5 to −408.4 MPa and SDV15 spanning −29.7 to 19.6 MPa, correlating $\sigma_{sim} = -410.7$ MPa and $\tau_{sim} = -4.1$ MPa of Table 5. The near-symmetric magnitude of the SDV12 range relative to the P1 tensile value (414.4 MPa) provides direct visual confirmation of the near-symmetric tensile–compressive yield response of LENS-deposited IN625 discussed in Section 4.2.5, consistent with the small axial centre-shift encoded in the D_s coefficient of the calibrated Szczepiński surface.

Path P13, shown in Fig. 7(d), constitutes the most analytically informative case among the four contour sets. Despite targeting the same near-pure-shear direction as P5 ($|\ \alpha_{exp}\ | \approx 90°$), P13 exhibits the minimum experimental yield radius among all 17 paths ($r_{exp} = 278.5$ MPa), yet its SDV15 field spans −286.7 to −228.6 MPa and only 3.5% below the corresponding SDV15 range at P5. This apparent contradiction is resolved directly by the accumulated Armstrong–Frederick back-stress. Twelve prior sequential probes, weighted toward the tensile and positive-shear sectors have driven the α_{23} back-stress component toward

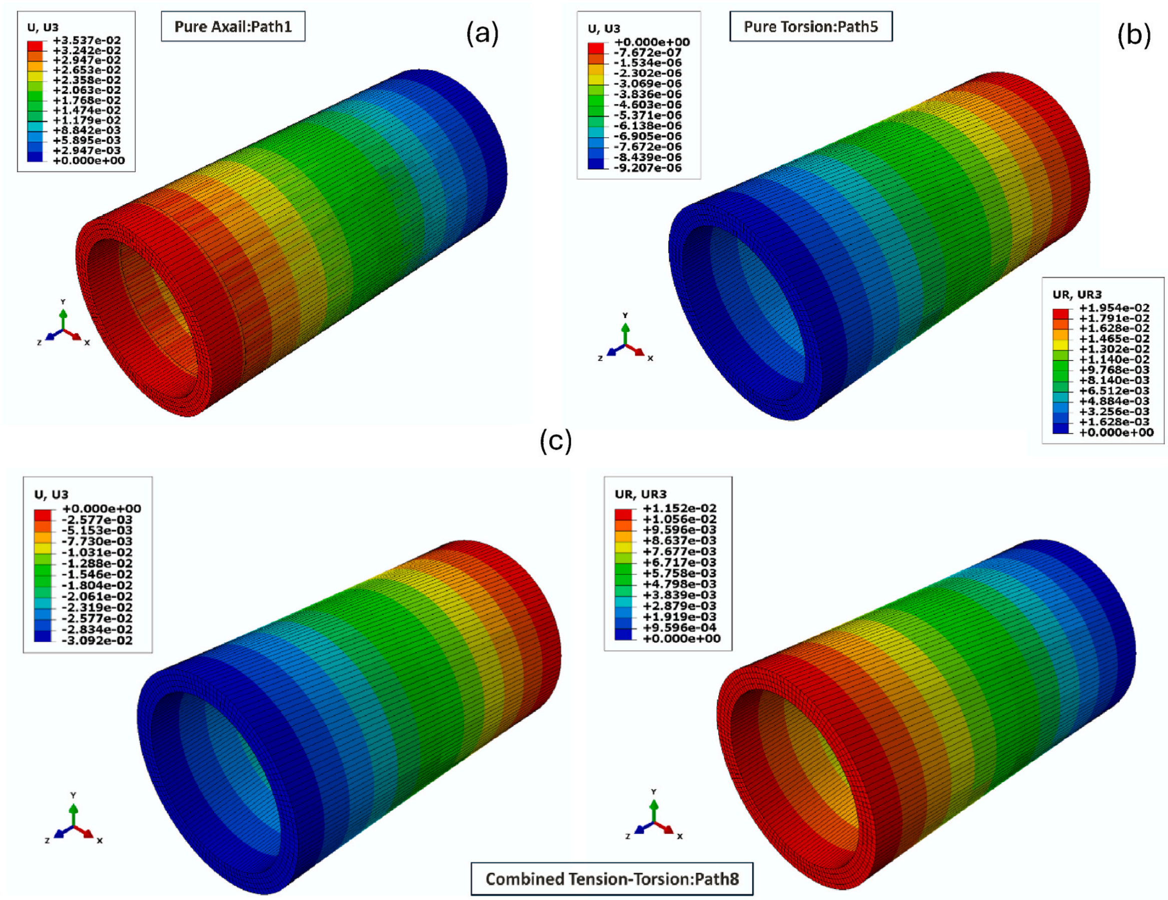

Fig. 6. Deformed model contours at the yield instant for three representative sequential loading paths: (a) P1, near pure tension (b) P5, near pure torsion and (c) P8, combined compression and torsion confirming deformation field homogeneity across the gauge section.

the negative-τ quadrant, translating the effective Szczepiński surface centre and elevating the local yield threshold above the virgin-surface prediction (r_{ell} = 286.6 MPa, Table 5) to the simulated value r_{sim} = 297.4 MPa (+6.8%, refer section 4.2.5). The elevated and spatially consistent SDV15 field in Fig. 7(d) therefore provides direct graphical, field-resolved evidence that the UMAT correctly retains and propagates the complete tensorial back-stress history across sequential paths.

Authors would like to emphasize that the simulated axial and torsional shear stress values in Table 5 are nominal and section-averaged stresses derived from the reaction force (RF3) and reaction moment (RM3) at the reference point, whereas the SDV12 and SDV15 contours represent local state-variable output distributed across the gauge-section wall thickness. The close correspondence between these two independently derived quantities across all four paths exact for P1, and within the physically expected through-wall gradient bound for P5, P9, and P13 confirms that the FE results are internally self-consistent.

4.2.6. *Simulated stress trajectories*

Table 5 presents the complete numerical output for all 17 paths simulations. The converged simulation angle α_{sim} and angular residual $\Delta\alpha = \alpha_{sim} - \alpha_{exp}$ quantify the directional accuracy achieved by the two-step boundary-condition correction and are discussed separately in Section 4.2.7. In Table 5, σ_{sim} and τ_{sim} are the actual Cauchy stresses at the yield instant, computed from reaction forces and moments at the first increment in which the cumulative equivalent plastic strain satisfies $\Delta\overline{\varepsilon}^p \geq 1 \times 10^{-4}$. These are the simulated yield points and constitute for quantitative comparison against the experimental data of Table 4. The scalar simulated yield radius is defined as $r_{sim} = \sqrt{\sigma_{sim}^2 + \tau_{sim}^2}$, consistent with the experimental definition $r_{exp} = \sqrt{\sigma_{exp}^2 + \tau_{exp}^2}$, both measuring the Euclidean distance from the stress-space origin to the respective yield surface in the (σ, τ) plane.

Authors would like to highlight that this geometric radius must not be confused with the Von Mises equivalent stress $\sigma_{VM} = \sqrt{\sigma^2 + 3\tau^2}$, which equals the uniaxial yield stress σ_Y only under the isotropic J_2 criterion, a formulation explicitly superseded here by the Szczepiński surface. The numerical difference between these two metrics can reach 73% in near-pure shear directions, making the choice of radius definition physically significant for every reported metric. The Szczepiński locus radius r_{ell} evaluated analytically at αsim and reported in the r_{ell} column of Table 5 is ellipse radius in the ideal radial direction at α_{sim}. Its sole function in Table 5 is to define the ellipse-boundary coordinates used exclusively to draw the analytical ellipse curve in Fig. 8 and must not be used in any quantitative comparison.

Fig. 8 presents the comparison of experimental and simulated material response under biaxial loading in the (σ, τ) plane. It can be clearly observed that the simulated stress trajectories closely follow the experimentally obtained responses for each loading path. The simulated stress trajectories were reconstructed from the reaction force and moment histories at every converged increment across all 17 sequential loading paths. Each trajectory originates from the residual stress state inherited from the preceding path's elastic springback and propagates radially outward toward the target probing direction α_{exp}, tracing the proportional displacement–rotation loading imposed by the boundary conditions.

The terminal point of each trajectory where the cumulative equivalent plastic strain first reaches $\Delta\overline{\varepsilon}^p = 1 \times 10^{-4}$ defines the simulated yield

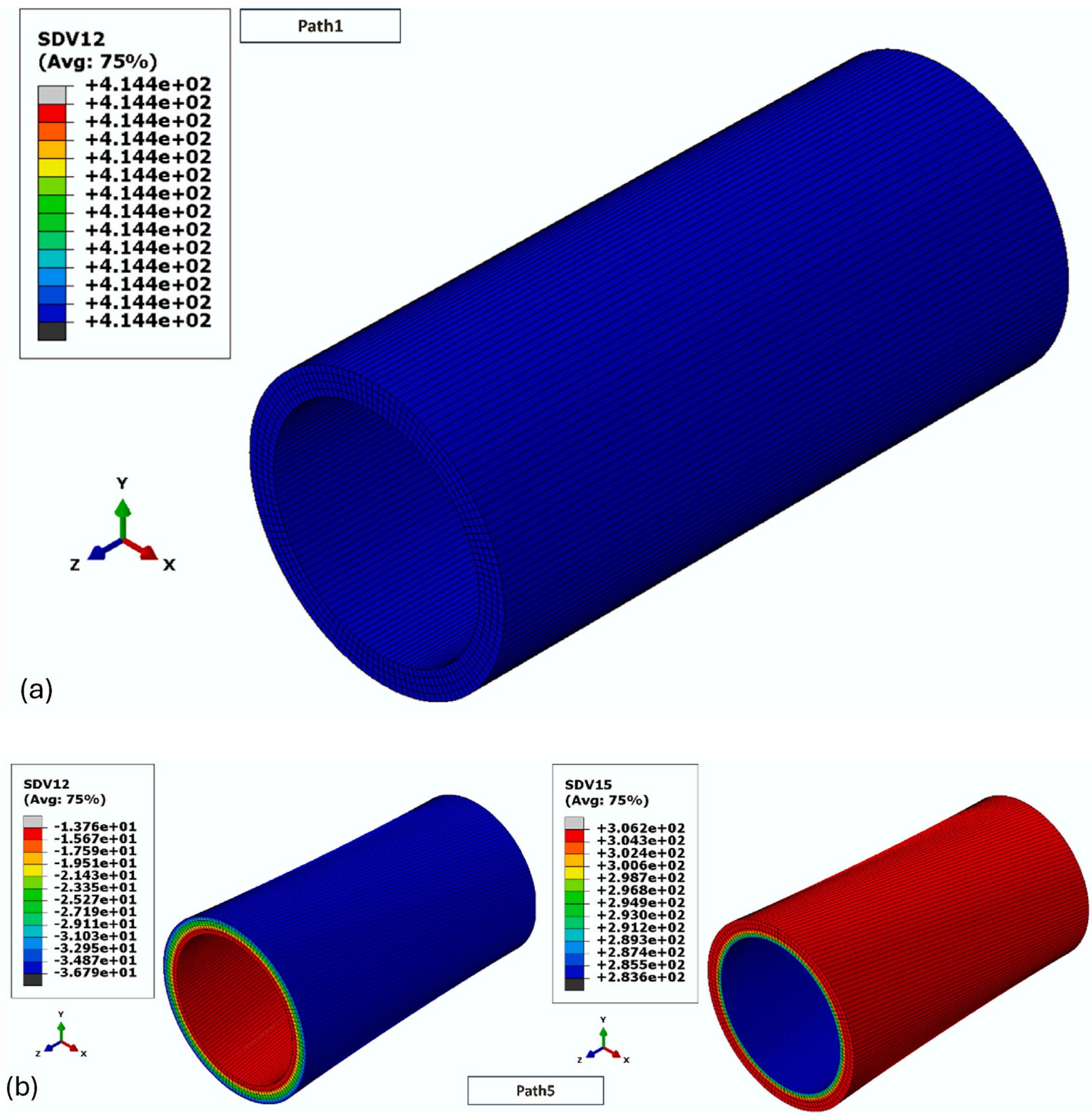

Fig. 7. Contour plots of the axial (SDV12) and torsional shear (SDV15) stress state variables at the 0.01% equivalent plastic strain offset for (a) Path P1 (near-pure tension), showing a spatially uniform value of 414.4 MPa across the gauge section, (b) Path P5 (near-pure torsion): SDV12 ranges from −36.8 to −13.8 MPa and SDV15 ranges from 283.6 to 306.2 MPa across the wall thickness, (c) Path P9 (near-pure compression): SDV12 ranges from −413.5 to −408.4 MPa and SDV15 ranges from −29.7 to 19.6 MPa, and (d) Path P13 (sequential negative shear, following twelve prior probing paths): SDV12 ranges from 3.4 to 28.8 MPa and SDV15 ranges from −286.7 to −228.6 MPa.

point from Table 5. The 17 trajectories collectively drawn over the full 360° spectrum of the biaxial stress space, covering near-pure tension (P1, P17), progressive tension–shear combinations (P2–P4), near-pure shear (P5), compression–shear (P6–P12), near-pure compression (P9), and the complementary shear–tension return paths (P13–P16). The spatial distribution of the 17 terminal points reproduces the anisotropic geometry of the Szczepiński yield surface, with r_{sim} ranging from 286 MPa for near pure shear to 414 MPa in the near-axial directions, consistent with the directional yield strength differential of LENS-deposited IN625. Nevertheless, all 17 trajectories exhibit a measurable opening angle between the forward loading branch and the reverse elastic springback upon force removal, as depicted from the enlarged view of stress trajectory in Fig. 8. This opening is smallest for near-axial paths (P1, P9, P17), where the axial–shear elastic coupling term is negligible, and largest for oblique and shear-dominant paths (P5–P7, P10–P13), where the anisotropic elastic compliance of the LENS-deposited IN625 crystallographic texture is fully engaged [1,2]. The directional back-stress components accumulated from the preceding sequential paths further amplify the opening angle in oblique paths via the multiaxial Bauschinger effect [7,11]. The non-parallel orientation of the forward loading branch and the reverse elastic springback path, most pronounced for paths P5–P7 and P10–P13, is a direct consequence of the path-dependent anisotropy of the back-stress tensor. The yield surface centre has migrated in the loading direction, and therefore, the elastic domain encountered during unloading is geometrically asymmetric relative to the applied stress vector.

The enlarged view of Fig. 8 also reveals that no unloading trajectory returns precisely to the stress-space origin point; the endpoints of the 17 springback paths are distributed within a region of approximately ±20 MPa in σ and ±15 MPa in τ-stress space, offset from the origin, with the

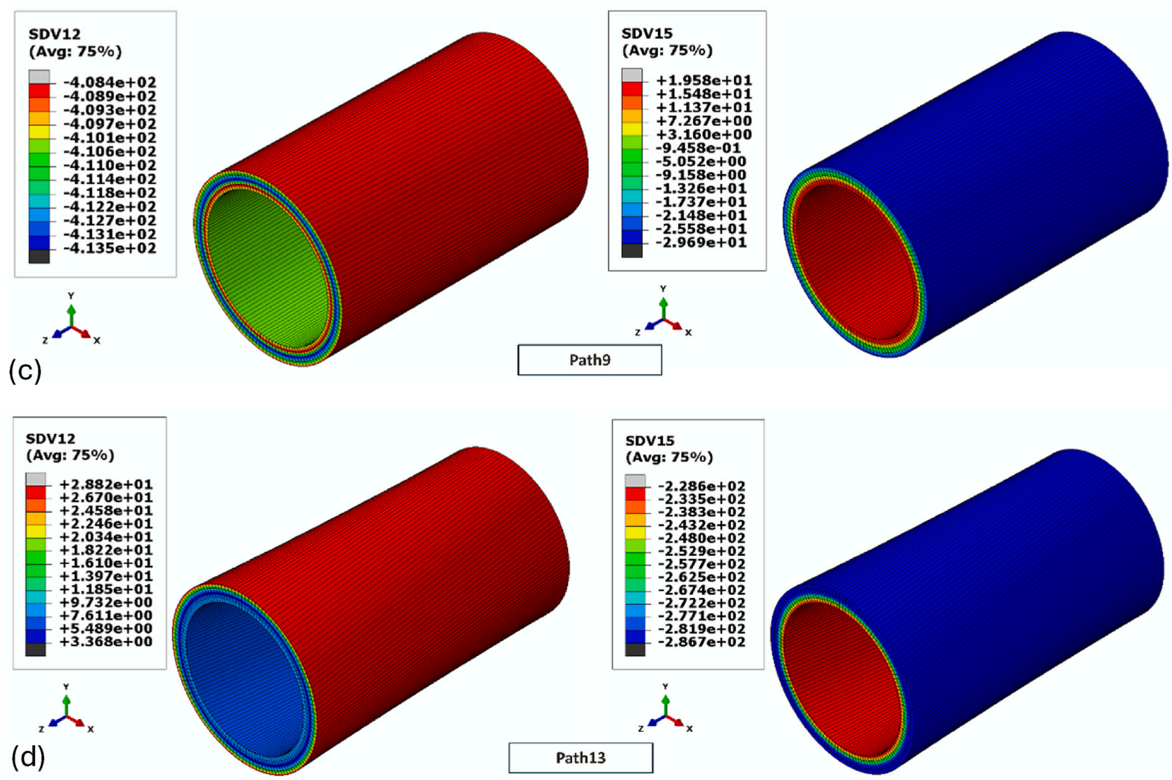

Fig. 7. (*continued*).

largest offsets in the compressive–shear paths (P6, P7, P10, P11). These non-zero residual stresses may arise from two coexisting physical mechanisms: (i) macroscopic self-equilibrating residual loads, where the elastic grip sections impose a constraining reaction on the plastically deformed gauge section upon actuator return, preventing complete stress relaxation [34]; and (ii) grain-scale intergranular residual stresses, where elastic low-Schmid-factor grains constrain the stress relaxation of adjacent yielded high-Schmid-factor grains, producing an intergranular back-stress that offsets the macroscopic mean stress from zero [35]. Evidently, the developed user subroutine UMAT reproduces both features within a single constitutive framework. The Armstrong–Frederick back-stress tensor accumulates direction-dependent components through each sequential probing step, governing the multiaxial Bauschinger rotation of the unloading branch, while the Szczepiński criterion determines the directional yield threshold at which departure from elastic springback begins. With the stress trajectories confirming that the simulated loading paths reach the intended directions across all sequential quadrants, the following section reconstructs the complete yield locus from the 17 terminal points and provides a direct geometric comparison against the analytically calibrated Szczepiński ellipse.

4.2.7. *Locus of yield surface and yield stress validation*

This section constitutes the primary experimental validation of the proposed UMAT framework, directly comparing all 17 simulated yield points of Table 5 against their experimental counterparts from Table 4 across the full 360° biaxial stress space. Fig. 9 presents the complete yield locus of LENS-deposited Inconel 625 in the (σ, τ) plane, superimposing the 17 experimental yield points from Table 4, the 17 simulated yield points from Table 5 and the Szczepiński analytical ellipse calibrated by least-squares optimisation against the experimental yield points. Notably, the Szczepiński ellipse achieves a calibration goodness-of-fit of 99% with an RMS error of 0.083 and a maximum absolute deviation of 0.112, confirming an excellent representation of the experimental data.

The fitted surface differs from the isotropic Huber-Von Mises-Hencky yield surface in three simultaneously observable and physically distinct ways. First, near-axial yield radii of approximately 401–418 MPa versus pure-shear radii of 279–291 MPa exhibiting shear-to-axial strength ratio approximately 0.72, substantially above the isotropic value of $1/\sqrt{3} \approx 0.577$. This confirms LENS-deposited IN625 is relatively stronger in shear than the isotropic prediction. Second, the ellipse centre is displaced from the stress-space origin by approximately (+48.5 MPa, −9.6 MPa) in stress plane, corresponded by the non-zero linear coefficients $D_s = -5.025 \times 10^{-7}$ and $F_s = -1.096 \times 10^{-4}$. This centre offset is the geometric signature of the net kinematic back-stress imparted by the LENS process, the positive axial shift reflects a tensile-sense residual stress introduced by thermal contraction of deposit layers upon cooling, while the negative shear shift reflects a systematic shear back-stress arising from crystallographic texture asymmetry about the deposition axis [14,20]. Third, the non-zero coupling coefficient $B_s = 4.147 \times 10^{-7}$ produces a measurable inclination of the Szczepiński ellipse principal axes relative to the (σ, τ) coordinate frame, indicating crystallographic shear coupling in the ⟨001⟩ textured columnar grains characteristic of LENS-deposited Nickel-based alloys [2,14,36]. The 17 simulated yield points cluster closely around the Szczepiński ellipse, confirming self-consistent triple agreement. The Szczepiński calibration accurately represents the experimental data, and the UMAT accurately reproduces the Szczepiński surface in the finite element simulation. The triple agreement between the experimental yield points, the calibrated Szczepiński ellipse and the simulated yield points sustained across all four quadrants of the biaxial stress space constitutes the primary quantitative validation of the proposed methodology against the experimental dataset of Table 4.

This section decomposes the overall locus agreement into its scalar constituent components to identify directional accuracy patterns across all 17 probing paths. Fig. 10(a)–(c) present the comparison between experimental and FE yield stresses and yield radii across all 17 sequential probing directions for LENS-processed IN625. For enhanced

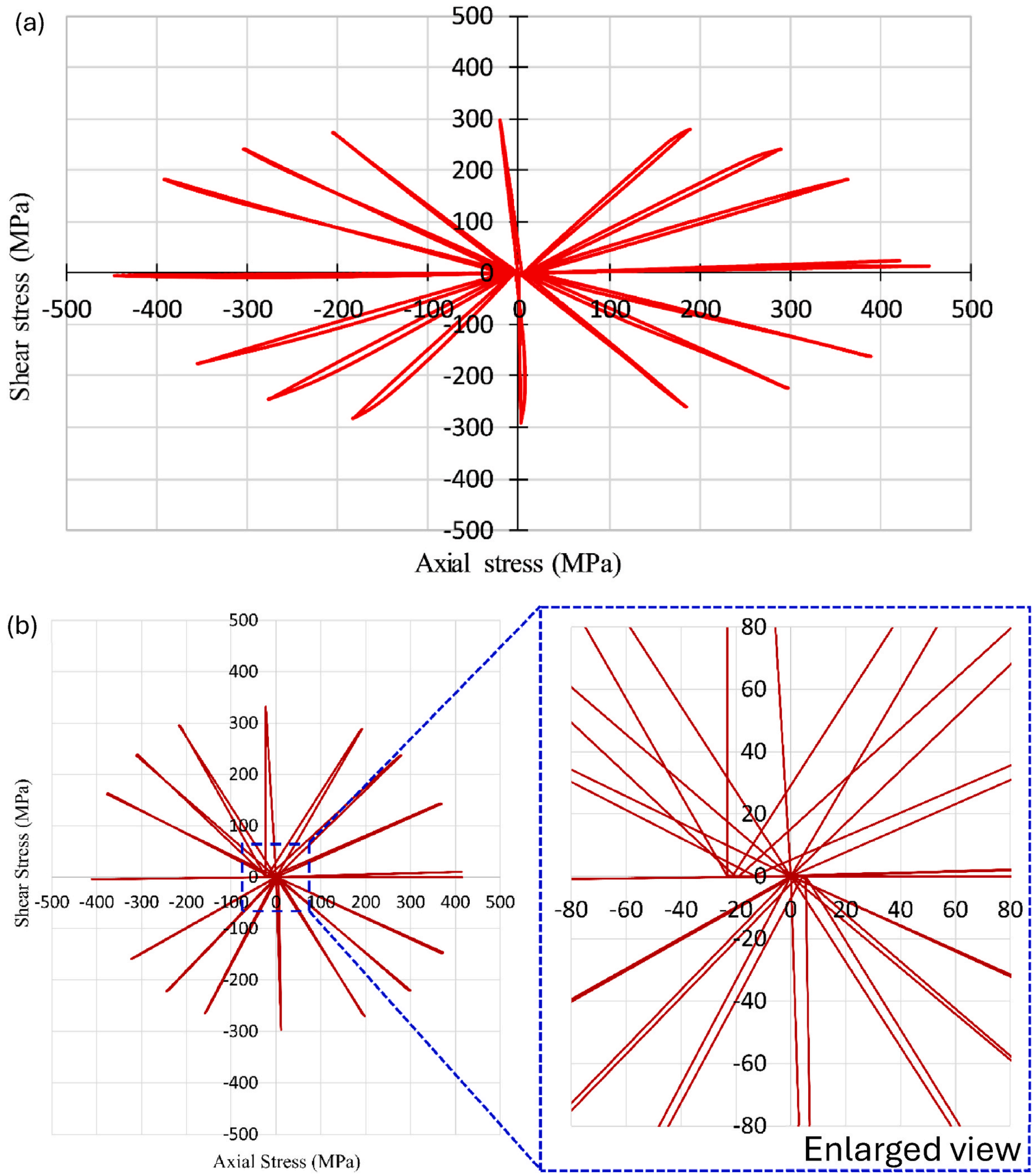

Fig. 8. (a) Experimental and (b) simulated stress trajectories in the (σ, τ) stress plane for all 17 sequential biaxial loading paths of LENS-deposited IN625 alloy. Enlarged view of the elastic springback trajectories highlights the non-zero residual stress offsets upon unloading.

visualization, Fig. 10(a)–(c) decompose the yield surface validation into three scalar graphical plots: axial stress, shear stress, and scalar yield radius, $= \sqrt{\sigma^2 + \tau^2}$, providing a path-resolved, component-level accuracy assessment.

Fig. 10(a) presents the axial stress component at yield for all 17 sequential probing paths. Both experimental and simulated stress profiles exhibit the expected co-sinusoidal variation with loading angle confirming the full sign reversal of the axial stress component across the 360° probing plane. The experimental axial stress ranges from −404.3 MPa at P9 (near-pure compression) to +401 MPa at P1 and at P17 (near-pure tension) (Table 4). The corresponding simulated values reproduce the same trend, ranging from −410.7 MPa at P9 to +414.2 MPa at P1 and +413.4 MPa at P17 (Table 4). The UMAT subroutine reproduces both sign and magnitude of σ consistently across all four loading quadrants, with a mean absolute deviation $|\Delta\sigma| = 11.4$ MPa corresponds to a relative error of 9.8%. The largest discrepancy arises at P10 ($|\Delta\sigma| = 32.0$ MPa), followed by P14 ($|\Delta\sigma| = 22.5$ MPa) and P6 ($|\Delta\sigma| = 17.2$ MPa). These three paths share a common physical origin rooted in loading direction reversal relative to the accumulated back-stress vector. At P10, the loading direction enters the compressive–negative shear quadrant for the first time after nine preceding paths concentrated in the positive-shear sectors, maximising the angular misalignment between the accumulated back-stress tensor and the new probing direction, and producing the largest axial deviation. At P14 and P6, the oblique loading directions cross the σ-axis at angles where the axial back-stress component most strongly opposes the applied σ, yielding deviations of 22.5 MPa and 17.2 MPa, respectively. By contrast, paths with large number of prior loading histories but near-axial or near-pure-shear

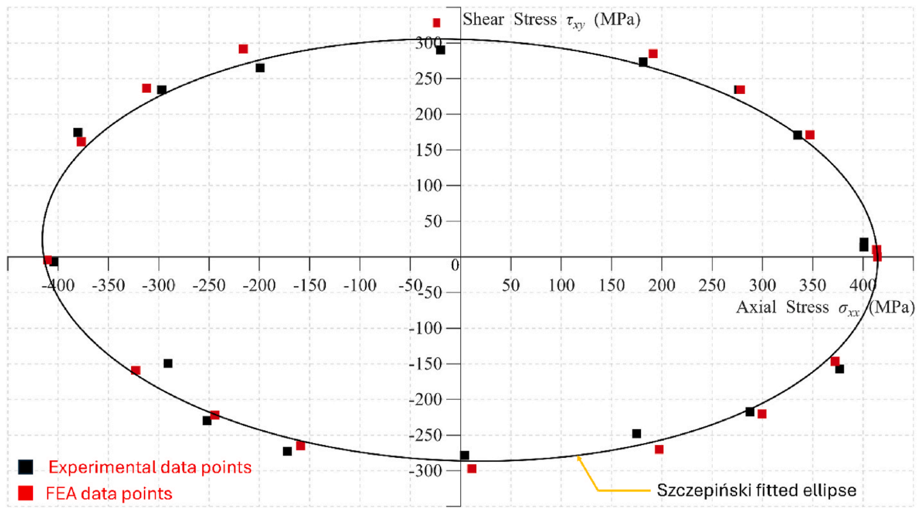

Fig. 9. Experimental and simulated yield points of LENS-deposited IN625 in biaxial (σ, τ) stress plane along with Szczepiński analytical ellipse.

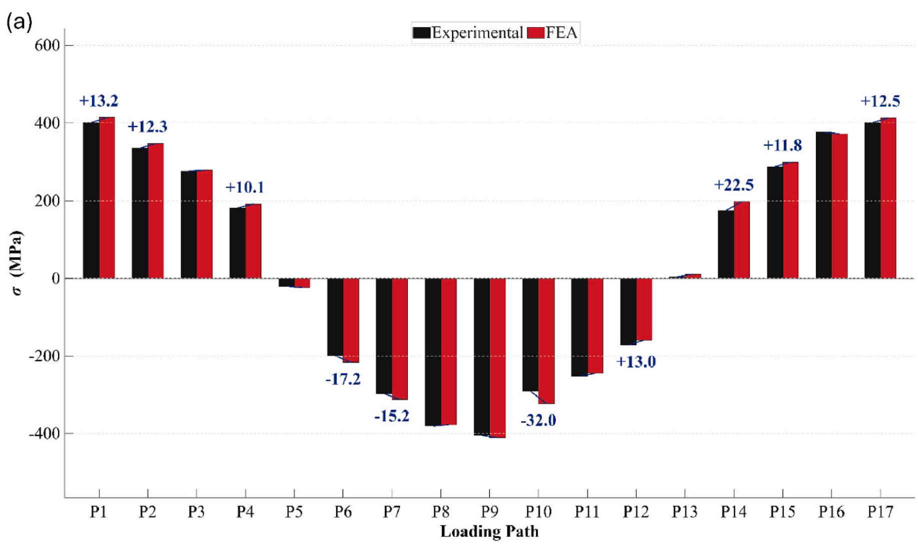

Fig. 10(a). Path-resolved comparison of axial stress between experimental and simulated yield stresses across all 17 sequential loading paths for LENS-deposited IN625.

orientations such as P16 (15 prior paths, $|\Delta\sigma| = 4.3$ MPa) and P13 (12 prior paths, $|\Delta\sigma| = 7.2$ MPa) exhibit small deviations, because the back-stress direction closely aligns with the current probing direction, reducing the net axial threshold shift. This confirms that the dominant driver of path-to-path variation in axial stress accuracy is the angular misalignment between the accumulated Armstrong–Frederick back-stress tensor and the current probing direction instead of cumulative number of prior paths. The spatial concentration of the largest axial deviations in the compressive–negative shear and oblique-return sectors is therefore physically deterministic and directionally reproducible.

On similar pattern, Fig. 10(b) presents the shear stress component at yield. Both profiles exhibit a complementary sinusoidal pattern, with highest shear stress ±(290-332) MPa for near-torsional paths (P5, P13) and approaching zero at the near-axial paths (P1, P9, P17). The UMAT reproduces the directional shear response with $|\Delta\tau| = 12.5$ MPa across all 17 paths. The single largest discrepancy occurs at P5 ($|\Delta\tau| = 41.4$ MPa, +14.2%), where two associated effects simultaneously reach their maximum: (i) the Szczepiński ellipse bulges furthest beyond the Von Mises yield surface, amplifying the sensitivity of τ_{sim} to any residual angular error; and (ii) the accumulated back-stress from paths P1–P4 has already shifted the elastic domain, requiring the highest angular correction ($\Delta\alpha_1 = +13.2^\circ$ at P5) and introducing the greatest residual angular uncertainty in τ_{sim}. The grey connector lines between each experimental–simulation bar pair confirm that the directional character of the shear response is reproduced consistently across the full angular span with no systematic sign error in any quadrant.

Fig. 10(c) presents the scalar yield radius alongside the percentage deviation Δr(%) on the right ordinate axis. The experimental yield radii span from 278.5 MPa to 418.4 MPa, reflecting the directional variation of the Szczepiński anisotropic criterion, with maxima in the near-axial directions and a clear minimum near pure shear (P13). Among the 17 simulated paths, seven fall within the ±3% excellent agreement band, nine fall inside the ±3%–7% acceptable band, and one path P10 falls outside the ±7% tolerance yielding an overall path-averaged MAE of 3.6%. The four paths with the largest radial deviations P5 (+14.3%), P10 (+10.0%), P13 (+6.8%), and P2 (+3.6%) are all located in the intermediate-angle regime ($45^\circ \le |\alpha| \le 135^\circ$), where cumulative kinematic back-stress from the preceding sequential paths most strongly elevates the effective yield threshold beyond the as-calibrated Szczepiński surface.

These two largest single-component deviations can also be expressed as a fraction of the experimental yield radius instead of the full vector

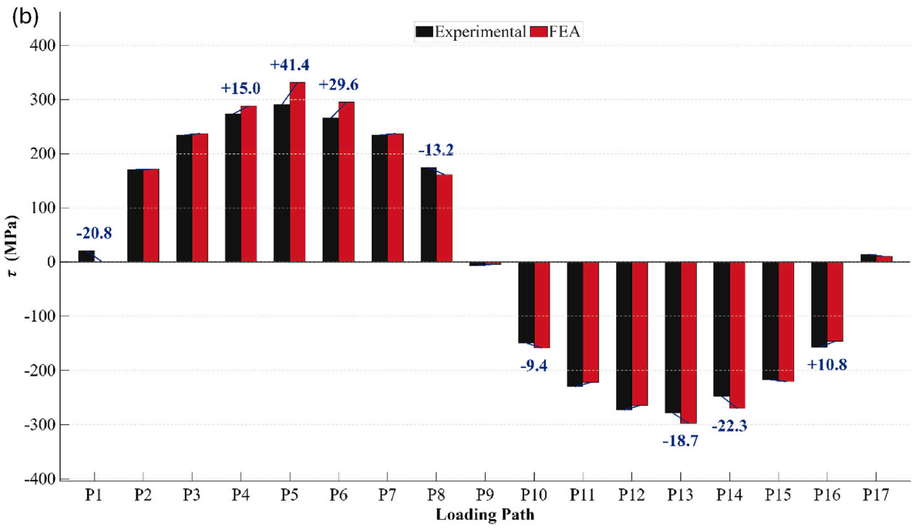

Fig. 10(b). Path-resolved comparison of shear stress between experimental and simulated yield stresses across all 17 sequential loading paths for LENS-deposited IN625.

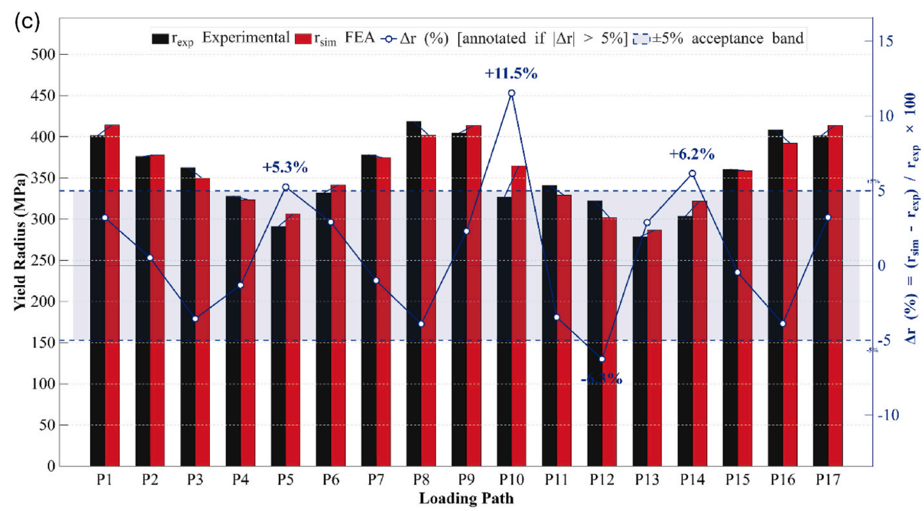

Fig. 10(c). Path-resolved comparison of scalar yield radius with percentage deviation Δr (%) on the right ordinate between experimental and simulated yield stresses across all 17 sequential loading paths for LENS-deposited IN625.

magnitude. On this basis, P10 (axial) shows a component-wise relative error of approximately 9.8%, using $r_{exp} = 327$ MPa. P5 (shear) shows a component-wise relative error of approximately 14.2%, using $r_{exp} = 291$ MPa. Both values are consistent with the overall radial deviations of $+10.0\%$ and $+14.3\%$ reported above for the same two paths. The small numerical difference arises because the component-wise ratio considers only one stress component, σ or τ, in the numerator. In contrast, $\Delta r(\%)$ accounts for the full vector magnitude of both components combined. Having established the component-wise accuracy profile, the next section presents the normalised convergence metrics that provide a path-level scalar summary of both the radial and angular accuracy across the full sequential probing protocol.

4.2.8. *Normalised yield radius and angular convergence*

To provide a path-resolved scalar accuracy metric independent of the stress component decomposition, Fig. 11 presents the normalised yield radius ratio r_{sim}/r_{exp} for all 17 loading paths, with superimposed $\pm3\%$ (excellent) and $\pm7\%$ (acceptable) tolerance bands. Values above unity indicate radial overprediction and below unity indicate underprediction.

Seven paths fall within the $\pm3\%$ excellent band. A directionally coherent trend is apparent for paths in the tensile-dominant quadrant (P1–P4) exhibiting a mild systematic overprediction within $r_{sim}/r_{exp} \in [1.005, 1.053]$. However, compression, oblique, and near-axial return paths (P8, P11–P12, P16) show a corresponding systematic underprediction within $r_{sim}/r_{exp} \in [0.937, 0.964]$, yielding a path-averaged MAE of 3.64%. This directional asymmetry is consistent with the anisotropic yield strength differential between the tensile and compressive loading regimes of the LENS-deposited microstructure and with the asymmetric saturation of the Armstrong–Frederick back-stress across the sequential probing procedure. Path P10 alone yields $r_{sim}/r_{exp} = 1.10$ (+10%), attributable to the maximum accumulated back-stress magnitude attained after nine prior paths loading predominantly the compressive and shear sectors, rotating and distorting the elastic domain beyond the corrective capacity of the two-step angle correction strategy. Notwithstanding this single outlier, 16 of 17 paths converge within $\pm7\%$, and the path-averaged MAE of 3.6% confirms that the Szczepiński-UMAT framework captures the anisotropic yield surface topology with excellent overall accuracy across the complete biaxial stress space.

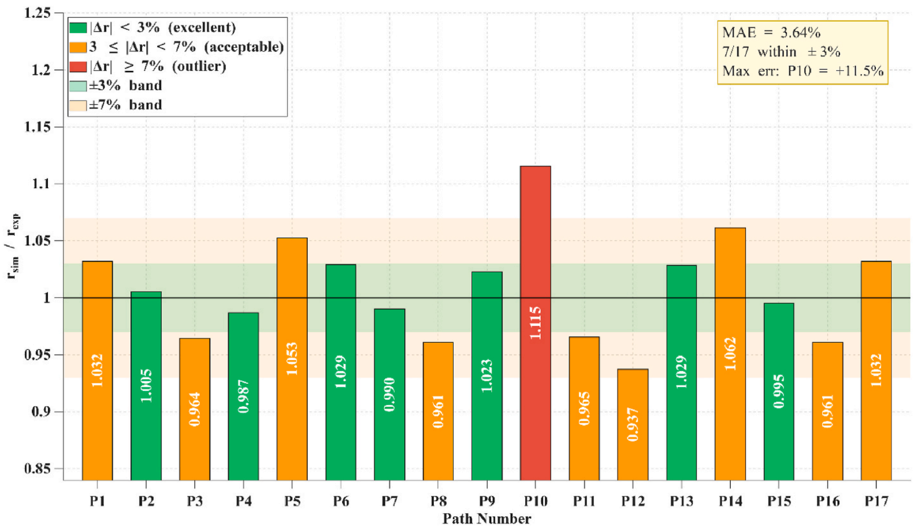

Fig. 11. Normalised yield radius ratio r_{sim}/r_{exp} for all 17 sequential loading paths, with ±3% and ±7% tolerance bands.

Complementing the radial assessment, Fig. 12 presents the angular convergence performance of the two-step boundary-condition correction strategy. Prior to correction, the Run-1 errors range from 7.8° at P12 to 13.2° at P5, with a Run-1 MAE of 6.05°.

A 13.2° Run-1 angular overshoot at P5, if uncorrected, would displace the simulated yield point by approximately $| r_{ell} \cdot \sin(13.2°)|$ nearly 70 MPa from the targeted locus completely diverting the shear-dominant branch of the yield surface and demonstrating the critical necessity of the correction strategy. The two-step correction reduces these errors significantly, with MAE dropping to 0.86°, an 86% reduction, and 16 of 17 paths satisfy the $| \Delta\alpha | \leq 1.5°$ acceptance criterion. As depicted, Path P1 retains a residual of $\Delta\alpha = -2.97°$, attributed to the virgin specimen condition at the start of P1 no prior back-stress is available to correct against, and the angular error is governed solely by the initial elastic anisotropy coupling. Since there is no prior back-stress history and the UMAT was developed from the Szczepiński ellipse co-ordinate point which is equal to the shift of the virgin elastic compliance, no correction run was performed. Paths P9 and P11 achieve final residuals of −0.4° and −0.1°, respectively, within the ±0.5° excellent band confirming the robustness of the correction algorithm across varied loading directions. With both radial and angular accuracy validated numerically, the following three sections present a three-dimensional characterisation of the anisotropy structure that has governed all of the path-level observations presented above.

4.2.9. Three dimensional proportional loading trajectory

The two-dimensional yield locus of Fig. 9 and the bar charts of Fig. 10 quantify the accuracy of the UMAT at the yield-surface boundary. However they do not reveal the dynamic loading mechanism by which each simulated yield point is reached. Fig. 13 extends the two-dimensional locus view by presenting the three-dimensional (3D) proportional loading trajectories for all 17 paths in the extended space (σ, τ, f), where the vertical axis $f = r(\alpha)/r_{VM}(\alpha)$ is the Szczepiński yield function normalised by the isotropic reference radius, so that $f = 1$ corresponds to the Von Mises isotropic yield threshold. Further, $f > 1$ indicates a direction stronger than the Von Mises prediction and $f < 1$ indicates a sub-isotropic direction. Each trajectory starts at the common stress-space origin and propagates radially outward in the (σ, τ) plane while ascending monotonically along the f-axis as elastic loading builds toward the yield boundary, forming the characteristic conical fan-shaped geometry observed in Fig. 13. The iso-f contour rings drawn at $f = 0.25$, 0.50, and 0.75 reveal the sub-yield scaling of the Szczepiński ellipse.

The non-circular in-plane geometry widest in the near-axial

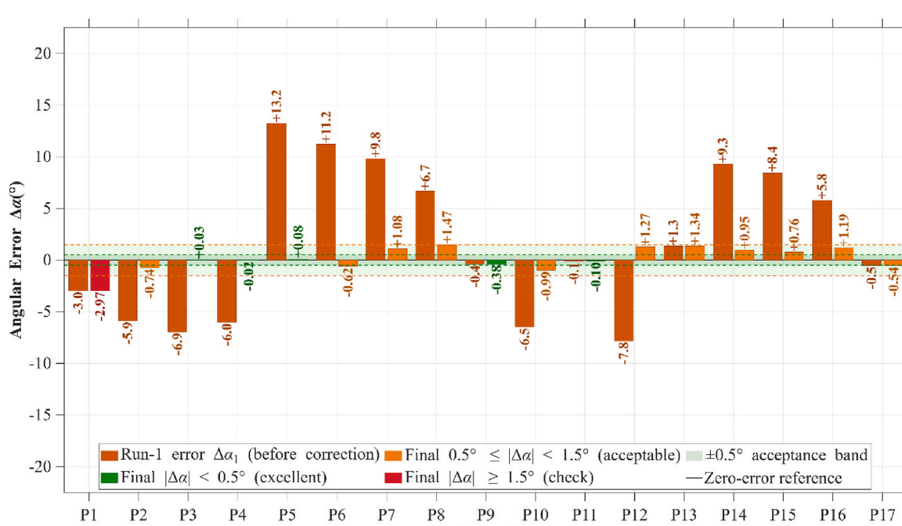

Fig. 12. Angular convergence of the two-step boundary condition correction strategy across all 17 sequential loading paths.

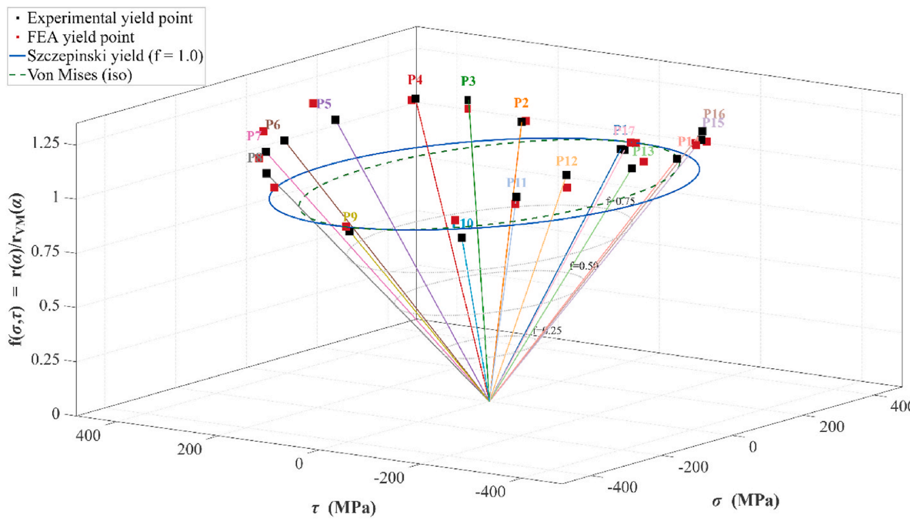

Fig. 13. Three-dimensional proportional loading trajectories for all 17 sequential probing paths in the extended (σ, τ, f) space for LENS-deposited IN625 alloy.

directions and narrowest in the shear directions demonstrates that the yield function iso-surfaces are geometrically self-similar ellipses at all loading levels, however, with a non-uniform directional scale factor, a direct consequence of the eccentric, inclined Szczepiński ellipse geometry. The experimental yield points span $f_{exp} \in [0.940, 1.223]$ across the 17 directions, confirming a total directional anisotropy range of 0.283 in the normalised yield function that explicitly disqualifies any isotropic yield criterion as a valid descriptor for this material.

The FEA yield points cluster near $f_{sim} \in [1.000, 1.279]$, and their close spatial co-location with the experimental terminal points provides a three-dimensional, visually unambiguous validation of the UMAT directional accuracy that cannot be achieved from either a 2D locus plot or a component bar chart alone. This 3D view of the loading mechanics motivates a direct quantification of the departure of the Szczepiński surface from the isotropic reference at every angular position, presented in the following section as a continuous three-dimensional deviation landscape.

4.2.10. Three dimensional anisotropy deviation surface

While Fig. 13 conveys the loading dynamics of each path, it does not directly isolate the magnitude and spatial distribution of the anisotropy itself. Fig. 14 addresses this by presenting the 3D deviation surface $\Delta r(\alpha) = r_{ell}(\alpha) - r_{VM}(\alpha)$, where $r_{ell}(\alpha)$ is the Szczepiński locus radius and $r_{VM}(\alpha)$ is the Von Mises reference radius, both evaluated as continuous functions of the probing angle α over the full 360° stress spectrum. A positive Δr indicates a direction where LENS-deposited IN625 is stronger than the isotropic prediction whereas a negative Δr indicates a sub-isotropic direction.

The orange displacement arrows shown in Fig. 14 connecting each experimental yield point to its corresponding simulated surfaces in the deviation-surface plane have a mean length of 12.9 MPa and reach a maximum of 34.3 MPa at P10 spatially and quantitatively consistent with the component-wise deviations. The spatial coherence of the largest arrows at P5 and P10 confirms that the residual discrepancies arise from the deterministic mechanism of back-stress saturation in the intermediate-angle quadrants rather than from randomly distributed numerical error. The deviation surface exhibits an approximate bilateral symmetry about the normal stress axis which is a consequence of the near-symmetric tensile and compressive yield radii of LENS-deposited IN625 in the near-axial directions, while the non-zero coupling coefficient $B_s = 4.147 \times 10^{-7}$ breaks τ-axis symmetry by inclining the Szczepiński ellipse principal axes relative to the coordinate frame, producing a monoclinic characteristics. Elevated yield radii in the off-axis tension–shear and compression–shear segments along with reduced radii along the pure-axial directions can be visualised from Fig. 14. Having characterised the full three-dimensional deviation profile, the

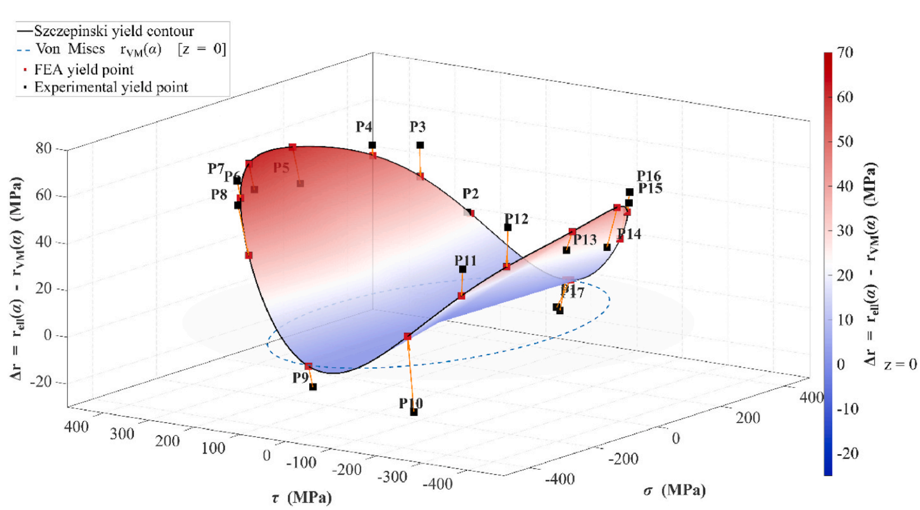

Fig. 14. Three-dimensional anisotropy deviation surface for LENS-deposited IN625 alloy evaluated continuously over the full 360° biaxial stress space for all 17 paths.

final section distil this directional information into a single scalar anisotropy index per probing direction, providing the most compact and interpretable summary of the yield surface anisotropy.

4.2.11. Directional anisotropy rose

Fig. 15 presents the Anisotropy Rose for LENS-deposited IN625, constructed by plotting the dimensionless anisotropy index, $\mathrm{AI}(\alpha) = r_{\mathrm{exp}}(\alpha)/r_{\mathrm{VM}}(\alpha)$ for each of the 17 probing directions as a polar radial band, colour-coded on a red–yellow–green scale. Deep green ($\mathrm{AI}(\alpha) > 1.05$, stronger than isotropic), yellow ($\mathrm{AI}(\alpha) \in [0.97, 1.05]$, near-isotropic), and red ($\mathrm{AI}(\alpha) < 0.95$, sub-isotropic). Among 17 paths, 13 fall in the deep green regime confirming that LENS-deposited IN625 is directionally stronger than the isotropic Von Mises prediction across the majority of the biaxial stress space. Three paths P1, P9, and P17 (all near-pure axial loading) fall in the yellow near-isotropic band, consistent with the calibration assumption in which the Von Mises reference radius is normalised by the uniaxial yield stress. The sole red zone at P10 with $\mathrm{AI}(\alpha) = 0.940$ represents the single direction in which the material falls measurably below the isotropic reference. Its spatial confinement between yellow-band neighbours P9 and P11 confirms a localised directional deficit attributed to the back-stress saturation mechanism identified in Section 4.2.7. The total directional spread $\Delta\mathrm{AI}(\alpha) = 1.223 - 0.940 = 0.283$ (28.3%) far exceeds the ±5% Von Mises tolerance band by a factor of 2.8. This demonstrates the unequivocal quantitative evidence that the LENS process introduces plastic anisotropy of a magnitude that renders isotropic yield criteria physically inadequate for this class of nickel-based alloys.

The three near-axial paths (P1, P9, P17) correctly appear as yellow (near-isotropic) bands because along the build axis the columnar grain orientation and the approximately symmetric Schmid factor distribution together drive the macroscopic yield stress toward the isotropic limit, with only a marginal 2.5% discrepancy attributable to inter-layer defects and axial tensile residual stress. The sole red zone at P10 represents a localised directional deficit in the compression–shear sector, spatially confined between yellow-band neighbours P9 and P11, confirming it does not constitute a general compressive failure mode. A 5.1 percentage-point asymmetry between the positive-shear peak (P5, $\mathrm{AI}(\alpha) = 1.215$) and the negative-shear peak (P13, $\mathrm{AI}(\alpha) = 1.164$) reflects the off-centre-symmetric offset of the Szczepiński ellipse centre from the stress-space origin. The net kinematic back-stress imparted by the LENS thermal cycling is stronger in the positive-shear direction, rendering the positive-τ hemisphere marginally stronger than the negative-τ hemisphere, a physical signature of the LENS layer-by-layer deposition asymmetry that would be entirely invisible to any isotropic plasticity analysis. The close correspondence between the FEA-predicted and experimentally measured $\mathrm{AI}(\alpha)$ values with a mean absolute deviation of 0.030 and a maximum of 0.075 at P5 confirms that the Szczepiński-UMAT subroutine framework captures both the magnitude and the directional distribution of the yield surface anisotropy across the complete 360° biaxial stress space. The Szczepiński ellipse envelops the Von Mises reference by up to +22.3% in the oblique shear-dominant sector and falls below it by only −6.0% at the single confined direction P10, capturing the full 28.3% anisotropy span that is entirely invisible to any isotropic plasticity analysis. This establishes the proposed framework as a reliable computational tool for the multiaxial constitutive characterisation of AM-fabricated superalloys.

5. Conclusions

This work developed and validated a novel finite element framework for simulating the complete anisotropic yield surface evolution of LENS-deposited Inconel 625 (IN625) under 17 sequential tension/compression–torsion probing paths spanning the full 360° of the biaxial (σ, τ) stress space. A custom UMAT subroutine implementing the Szczepiński anisotropic quadratic yield criterion with Armstrong–Frederick nonlinear kinematic hardening was developed within ABAQUS software and thoroughly validated against experimentally measured yield loci. The following conclusions are drawn from this work.

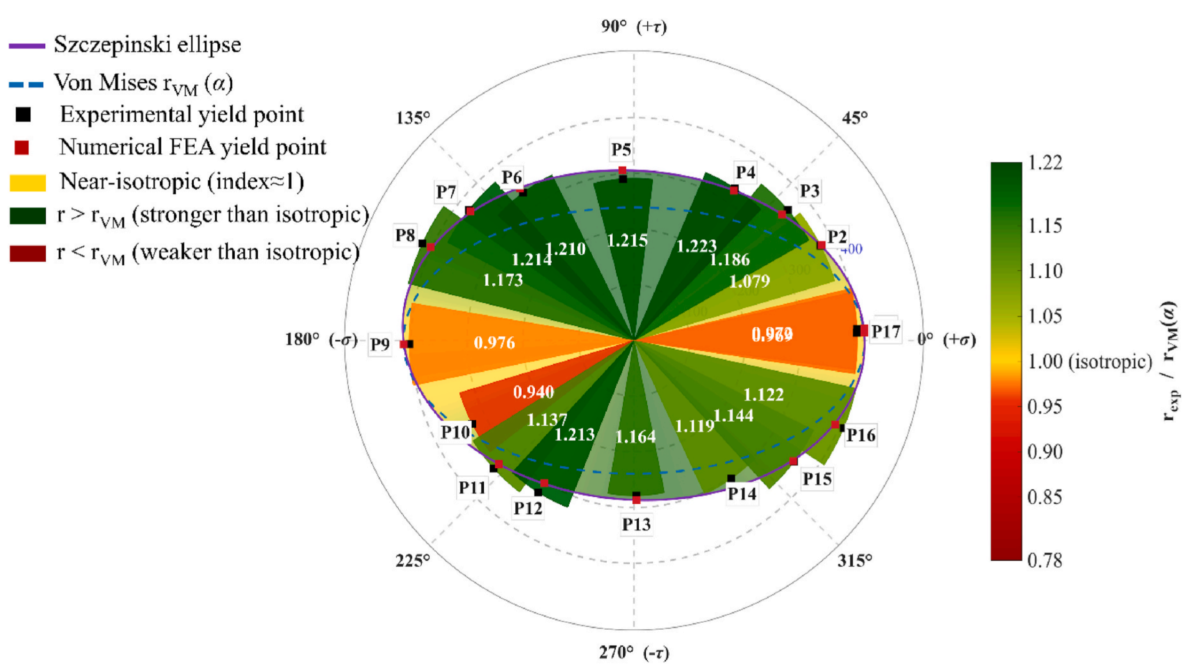

Fig. 15. Directional anisotropy rose for LENS-deposited IN625: polar plot of the anisotropy index, $\mathrm{AI}(\alpha)$ for all 17 probing directions. The peak anisotropy indices are $\mathrm{AI}(\alpha) = 1.223$ at P4 (+22.3%, combined tension–shear), $\mathrm{AI}(\alpha) = 1.215$ at P5 (+21.5%, near-pure shear), and $\mathrm{AI}(\alpha) = 1.214$ at P7 (+21.4%, compression–shear), forming a coherent deep-green arc spanning approximately $\alpha \in [27°, 156°]$ and $[-38°, -122°]$. This spatial pattern of directional strengthening is consistent with the ⟨001⟩//deposition-axis crystallographic fibre texture characteristic of LENS-fabricated Ni-base superalloys, in which the Schmid factors for primary {111}⟨110⟩ octahedral slip are maximised under oblique tension–shear and compression–shear loading relative to the pure-axial case, producing elevated directional resistance to plastic flow [2,3,19].

1. Conventional ABAQUS implementations that treat only the final Newton–Raphson correction as the total plastic multiplier systematically underestimate cumulative equivalent plastic strain, preventing reliable identification of the 0.01% offset yield point under sequential loading. The proposed accumulation scheme sums all incremental corrections across Newton–Raphson iterations to resolve this, enabling reliable yield-point identification across all 17 paths.
2. The Szczepiński anisotropic quadratic yield criterion was successfully coupled with Armstrong–Frederick nonlinear kinematic hardening within a UMAT user subroutine in ABAQUS software for LENS-fabricated AM alloys. The five-parameter calibration achieved 99% goodness-of-fit with RMS error of 0.083, capturing simultaneously the ellipse centre-shift, distortion, and inclination that J_2-based isotropic models fundamentally cannot reproduce.
3. The two-step iterative boundary condition correction reduced the mean angular residual from 6.05° (uncorrected) to 0.86° (corrected), with 16 of 17 paths satisfying $|\Delta\alpha| \leq 1.5°$. Path P1, applied to the virgin specimen with no prior back-stress history, retains a residual of −2.97°, an inherent constraint of single-specimen sequential probing methodology. Proportional displacement-controlled loading without angular correction systematically misdirects the probing angle by up to 13.2° due to accumulated kinematic back-stress from prior sequential paths.
4. A total yield radius spread of $\Delta AI(\alpha) = 28.3\%$ was resolved across the biaxial stress space, with peak anisotropy indices of $AI(\alpha) = 1.223$ at P4 (tension–shear) and $AI(\alpha) = 1.215$ at P5 (near-pure shear) values 2.8 times the ±5% tolerance band of the Von Mises criterion. This directional pattern is consistent with the maximum Schmid factor of the {111}⟨110⟩ octahedral slip systems aligned with the ⟨001⟩// deposition-axis fibre texture of LENS-deposited IN625.
5. This work's contribution lies not in the constitutive formulation itself, since anisotropic yield criteria and kinematic hardening laws have independent precedent in the literature, but in the validated application of the Szczepiński–Armstrong–Frederick combination within a forward-predictive ABAQUS UMAT for the specific material system and loading protocol of LENS-deposited IN625 under full 360° sequential biaxial probing.
6. The core algorithmic components are the Szczepiński yield function, the shifted-stress return-mapping algorithm, and the Armstrong–-Frederick nonlinear kinematic hardening law formulated entirely in terms of calibrated material constants. None of these parameters encode IN625-specific slip system geometry, crystallographic texture, or phase content, making the subroutine architecture reusable across alloy systems. This structural reusability however, represents an architectural property of the subroutine rather than a demonstrated predictive capability for other alloys.

6. Future scope

The extensibility of the present framework to a new material requires that its experimentally identified yield locus retain a quadratic (elliptical) form, as verified in the present work for IN625 with 99% goodness of fit (RMS error 0.083). Materials such as IN718 (γ'/γ'' precipitation strengthening), Ti–6Al–4V (HCP crystallography with tension-compression asymmetry), and SS316L (deformation-induced martensitic transformation) may produce yield loci that deviate from this quadratic form, requiring independent verification, and potentially extension of the Szczepiński formulation itself, before the same UMAT architecture can be applied. Accordingly, the framework's applicability beyond LENS-deposited IN625 should be regarded as a structurally justified but experimentally unverified capability, not a validated result of the present study. Sequential probing characterisation of LENS-deposited IN718 is currently in progress and will be reported in a forthcoming study to test this hypothesis directly.

Funding information

This work was funded by National Science Centre, Poland through the Grant No. 2023/51/B/ST8/01751.

Declaration of competing interest

The authors declare that they have no known competing financial interests or personal relationships that could have appeared to influence the work reported in this paper.

Acknowledgements

The authors would like to express their gratitude to our dedicated technical employee Mr. Mirosław Wyszkowski and Mr. Andrzej Chojnacki for their kind help during the experimental part of this work.

References

[1] Dinda GP, Dasgupta AK, Mazumder J. Laser aided direct metal deposition of inconel 625 superalloy: microstructural evolution and thermal stability. Mater Sci Eng, A 2009;509:98–104.
[2] Hu Y, Lin X, Li Y, Ou Y, Gao X, Zhang Q, Li W, Huang W. Microstructural evolution and anisotropic mechanical properties of inconel 625 superalloy fabricated by directed energy deposition. J Alloys Compd 2021;870:159426.
[3] Chen F, Wang Q, Zhang C, Huang Z, Jia M, Shen Q. Microstructures and mechanical behaviors of additive manufactured Inconel 625 alloys via selective laser melting and laser engineered net shaping. J Alloys Compd 2022;917:165572.
[4] Dunne Fionn, Nik Petrinic. Introduction to computational plasticity. Oxford: OUP; 2005.
[5] W. Szczepinski, On deformation-induced plastic anisotropy of sheet metals, Arch Mech, 45(1) 3-38.
[6] Agius D, Wallbrink C, Kourousis KI. Efficient modelling of the elastoplastic anisotropy of additively manufactured Ti-6Al-4V. Addit Manuf 2021;38.
[7] Bauschinger J. Über die veränderung der elastizitätsgrenze und die festigkeit des eisens und stahls durch strecken und quetschen, durch erwärmen und abkühlen und durch oftmals wiederholte beanspruchungen. Mittheilungen aus dem Mechanisch-Technischen Laboratorium der Königlich Bayerischen Technischen Hochschule in München 1886;13:1–115.
[8] Buckley SN, Entwistle KM. The Bauschinger effect in super-pure aluminum single crystals and polycrystals. Acta Metall 1956;4:352–61.
[9] Mises RV. Mechanik der plastischen Formänderung von Kristallen. Z Angew Math Mech 1928;8:161–85.
[10] Prager W. A new method of analyzing stresses and strains in work-hardening plastic solids. J Appl Mech 1956;23.
[11] Frederick CO, Armstrong PJ. A mathematical representation of the multiaxial Bauschinger effect. Mater A T High Temp 2007;24.
[12] Hill R. A theory of the yielding and plastic flow of anisotropic metals. Proc R Soc Lond, Ser A Math Phys Sci 1948;193(1033):281–97.
[13] Dubey VP, Kopec M, Łazińska M, Kowalewski ZL. Yield surface identification of CP-Ti and its evolution reflecting pre-deformation under complex loading. Int J Plast 2023;167:103677.
[14] Przygucki H, Dubey VP, Durejko T, Przygucka D, Kowalewski ZL, Jóźwiak S, Kopec M. Experimental identification of the yield surface for inconel alloys manufactured by using laser engineered net shaping. Int J Adv Manuf Technol 2026;143(11):7379–88.
[15] Kopec M, Dubey VP, Pawlik M, Wood P, Kowalewski ZL. Experimental identification of yield surface for additively manufactured stainless steel 316L under tension–compression-torsion conditions considering its printing orientation. Manufacturing Letters 2024;41:28–32.
[16] Marjanovic R, Szczepinski W. Yield surfaces of the M-63 brass prestrained by cyclic biaxial loading. Arch Mech 1974;26(2):311–20.
[17] Miastkowski J, Szczepiński W. An experimental study of yield surfaces of prestrained brass. Int J Solid Struct 1965;1(2):189–94.
[18] Geng Y, Harrison N. Functionally graded bimodal Ti6Al4V fabricated by powder bed fusion additive manufacturing: crystal plasticity finite element modelling. Mater Sci Eng, A 2020;773:138736.
[19] Somlo K, Frodal BH, Funch CV, Poulios K, Winther G, Hopperstad OS, Børvik T, Niordson CF. Anisotropic yield surfaces of additively manufactured metals simulated with crystal plasticity. Eur J Mech Solid 2022;94:104506.
[20] Hu G, Zhang K, Huang S, Woody Ju J-W. Yield surfaces and plastic flow of 45 steel under tension-torsion loading paths. China Acta Mechanica Solida Sinica 2012;25 (4):348–60.
[21] Chaboche JL. Time-independent constitutive theories for cyclic plasticity. Int J Plast 1986;2:149–88.
[22] Lemaitre J, Dufailly J. Damage measurements. Eng Fract Mech 1987;28:643–61.
[23] Simo JC, Hughes TJR. Computational inelasticity. New York, NY: Springer; 1998. New York.
[24] Rice JR, Tracey DM. On the ductile enlargement of voids in triaxial stress fields. J Mech Phys Solid 1969;17(3):201–17.

[25] Bažant ZP, Oh BH. Crack band theory for fracture of concrete. Matériaux et Constructions 1983;16(3):155–77.
[26] Lemaitre J, Chaboche JL. Mechanics of solid materials. Cambridge University Press; 1994.
[27] Haber S, Berger MS. Multidimensional quadrature formulas and haar functions. 1969.
[28] Berger MS, Duvaut G, Lions JL. Les Inequations en Mecanique et en Physique, vol. 27. Dunod; 1973.
[29] Simo JC, Taylor RL. Consistent tangent operators for rate-independent elastoplasticity. Comput Methods Appl Mech Eng 1985;48(1):101–18.
[30] De Souza Neto EA, Perić D, Owen DRJ. Computational methods for plasticity: theory and applications. 2008.
[31] Lubliner J, Moran B. Plasticity theory. J Appl Mech 1992;59.
[32] Drucker DC. A more fundamental approach to plastic stress strain relations. In: InProc. 1st US natl. Congr. Applied mechanics; 1952. p. 487–91.
[33] Dubey VP, Kopec M, Przygucka D, Pawlik M, Wood P, Kowalewski ZL. Effect of the printing orientation on the yield surface and its evolution reflecting plastic pre-deformation of additively manufactured stainless steel 316L. Int J Adv Manuf Technol 2025;140(1):313–34.
[34] Kume R, Okabayashi H, Amano M. Mechanism of underclad cracking-combined effects of residual strain and heat-affected zone ductility, journal of engineering materials and technology. Transactions of the ASME 1976;98:348–56.
[35] Daymond MR, Bouchard PJ. Elastoplastic deformation of 316 stainless steel under tensile loading at elevated temperatures. Metall Mater Trans 2006;37(6):1863–73.
[36] Chen W, Chen C, Zi X, Cheng X, Zhang X, Lin YC, Zhou K. Controlling the microstructure and mechanical properties of a metastable β titanium alloy by selective laser melting. Mater Sci Eng, A 2018;726:240–50.